

KLF Analysis Report: Meson Spectroscopy Simulation Studies

Shankar Adhikari and Moskov Amaryan

Old Dominion University

August 7, 2020

Abstract

This analysis report is written as a supplemental for the strange meson spectroscopy part of the KLF proposal submitted to the JLab PAC48.

Contents

1	INTRODUCTION	1
2	K_L-FACILITY	4
3	PARTICLE IDENTIFICATION	7
4	DETAILS OF MC STUDY FOR $K_L p \rightarrow K^\pm \pi^\mp p$	8
4.1	$K^*(892)$ Production in KLF	10
5	DETAILS OF MC STUDY FOR $K_L p \rightarrow K^- \pi^0 \Delta^{++}$	14
6	DETAILS OF MC STUDY FOR $K_L p \rightarrow K_L \pi^- \Delta^{++}$	20
7	PARTIAL WAVE ANALYSIS	25
7.1	Partial wave analysis for neutral exchange	31
8	SYSTEMATIC UNCERTAINTIES	34
9	SUMMARY	35
A	Appendices	36
A.1	Generation Model For Monte Carlo Study	36
	References	39

1 INTRODUCTION

The simplest hadronic reaction that involves strange quark is $K\pi$ scattering, therefore its experimental study plays crucial role for our understanding of QCD in the non-perturbative domain. Theoretically the $K\pi$ scattering amplitude can be calculated based on Chiral Perturbation Theory at one loop [1, 2] and at two loops [3]. There are also LQCD calculations of $K\pi$ scattering from the first principles treatment of QCD [4, 5, 6, 7, 8, 9, 10, 11, 12].

For Chiral Perturbation Theory the interest is on the low energy parameters, particularly the scalar scattering lengths. But there is already quite discrepancy between existing measurements of ChPT [3, 13], dispersive analysis of experimental data [14, 15] and lattice calculation [7, 9, 16, 17]. Lack of experimental data below 750 MeV for $K\pi$ scattering is being a huge problem, where one needs an extrapolation down to the threshold at ≈ 635 MeV. Thus, the new KLF input at low energies, together with the general improvement in statistics, will settle this issue.

Another important motivation for $K\pi$ scattering amplitudes is the need to confirm the existence of the exotic κ meson (or $K_0^*(800)$ in the $I = 1/2$ S -wave. This state would be the strange counterpart of the σ (or $f_0(500)$) meson which is now rather well established from $\pi\pi$ scattering (see the review [18]).

The $K\pi$ scattering has two possible isospin channels, $I = 1/2$ and $I = 3/2$. For S -wave scattering, both are significant below 2 GeV, whereas the P -wave $I = 3/2$ is almost negligible. Below 1 GeV, the P -wave is basically a narrow elastic wave peaking at 892 MeV, interpreted as the $K^*(892)$ resonance, whereas a second resonance, the $K_1^*(1410)$ exists above 1 GeV, although its properties are less precisely known. The $I = 3/2$ S -wave is elastic and repulsive up to 1.7 GeV and contains no known resonances. The P -wave $I = 3/2$ has been measured in Ref. [19] and is also repulsive but very small. In case of $I = 1/2$ S -wave, it has a peaking broad resonance above 1350 MeV, interpreted as $K_0^*(1430)$. In addition, some phenomenological [20, 21, 22, 23, 24, 25, 26, 27, 28, 29, 30] and experimental [31, 32] studies suggest the presence of the κ resonance with a very large width, in the region close to the $K\pi$ threshold.

The best way to unravel these states and improve the current knowledge on them is to use elastic $K\pi$ scattering and perform partial wave analysis at the low t -Mandelstam variable to ensure scattering on a pion pole in the reactions $KN \rightarrow K\pi N$ or $KN \rightarrow K\pi\Delta$. In the past, charged kaon beams were used for this purpose. The K_L -facility will allow us to study $K\pi$ scattering using the neutral kaon beam through several reactions by charge and neutral exchanges. We performed simulation on some of those channels to obtain an insight on the precision measurement of partial waves and hence the κ pole calculation. Here are the channels we focus our simulation.

$$1. K_L p \rightarrow K^\pm \pi^\mp p \quad (1)$$

$$2. K_L p \rightarrow K^- \pi^0 \Delta^{++} \quad (2)$$

$$3. K_L p \rightarrow K_L \pi^- \Delta^{++} \quad (3)$$

The production mechanism for these channels includes charge and neutral exchanges. In particular at small momentum transfer region, $-t < 0.2 \text{ GeV}^2$, the amplitude is dominated by the one pion exchange contribution, see Fig. 1. Here the top panel is the Feynman diagram for a neutral pion exchange and the bottom panel for a charge pion exchange.

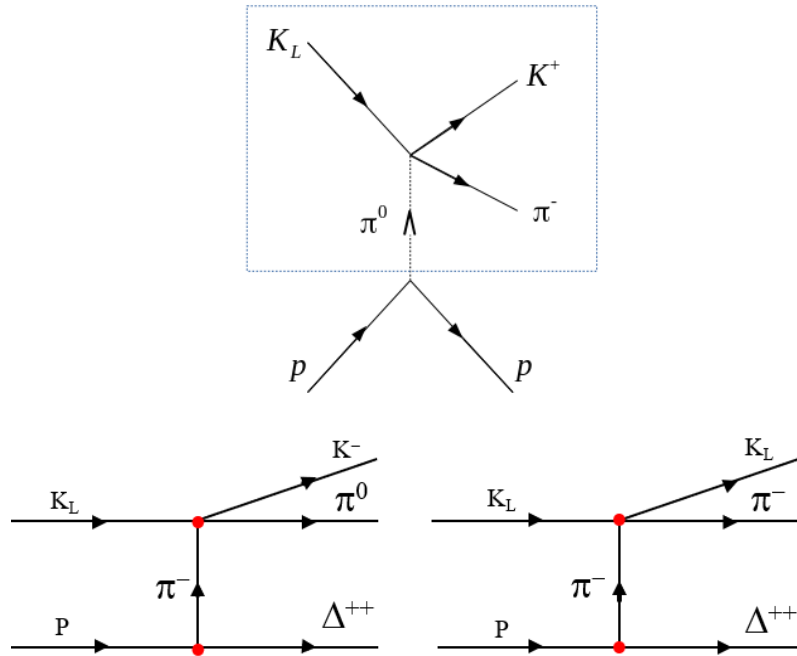


Figure 1: Illustration of the contribution from one-pion exchange, which is dominant at small momentum transfer, to the production amplitude. Top panel: $K_L p \rightarrow K^\pm \pi^\mp p$, Bottom Panel: $K_L p \rightarrow K^- \pi^0 \Delta^{++}$ (left), and $K_L p \rightarrow K_L \pi^- \Delta^{++}$ (right).

While the simulations described in this note have focused on the proton target data, similar reactions will be analyzed with the 100 days of deuterium target running. This

data will complement the proton target data and provide essential systematic checks on the extraction of the charged pion exchange contribution. In addition, the opportunity to study both proton and neutron target reactions at low t -Mandelstam will provide unprecedented access to all four isospin partners of $K^*(700)$ in a single experiment at KLF. To study the $K\pi$ system at KLF, a total of 18 production processes are possible, 9 for proton target and 9 for neutron target (listed in Eq. (4)) using K_L beam.

$$\begin{aligned}
K_L p &\rightarrow K^\pm \pi^\mp p = \langle K_L \pi^0 | K^\pm \pi^\mp \rangle = \pm \frac{1}{3} (T^{\frac{1}{2}} - T^{\frac{3}{2}}), \\
K_L p &\rightarrow K_L \pi^0 p = \langle K_L \pi^0 | K_L \pi^0 \rangle = \frac{1}{3} (T^{\frac{1}{2}} + 2T^{\frac{3}{2}}), \\
K_L p &\rightarrow K_{(L,S)} \pi^+ n = \langle K_L \pi^+ | K_L \pi^+ \rangle = \frac{1}{3} (T^{\frac{1}{2}} + 2T^{\frac{3}{2}}), \\
K_L p &\rightarrow K^+ \pi^0 n = \langle K_L \pi^+ | K^+ \pi^0 \rangle = -\frac{1}{3} (T^{\frac{1}{2}} - T^{\frac{3}{2}}), \\
K_L p &\rightarrow K^- \pi^0 \Delta^{++} = \langle K_L \pi^- | K^- \pi^0 \rangle = \frac{1}{3} (T^{\frac{1}{2}} - T^{\frac{3}{2}}), \\
K_L p &\rightarrow K_{(L,S)} \pi^- \Delta^{++} = \langle K_L \pi^- | K_L \pi^- \rangle = \frac{1}{3} (T^{\frac{1}{2}} + 2T^{\frac{3}{2}}), \\
K_L n &\rightarrow K^\pm \pi^\mp n = \langle K_L \pi^0 | K^\pm \pi^\mp \rangle = \pm \frac{1}{3} (T^{\frac{1}{2}} - T^{\frac{3}{2}}), \\
K_L n &\rightarrow K_L \pi^0 n = \langle K_L \pi^0 | K_L \pi^0 \rangle = \frac{1}{3} (T^{\frac{1}{2}} + 2T^{\frac{3}{2}}), \\
K_L n &\rightarrow K_{(L,S)} \pi^\pm \Delta^\mp = \langle K_L \pi^\pm | K_L \pi^\pm \rangle = \frac{1}{3} (T^{\frac{1}{2}} + 2T^{\frac{3}{2}}), \\
K_L n &\rightarrow K^\pm \pi^0 \Delta^\mp = \langle K_L \pi^\pm | K^\pm \pi^0 \rangle = \pm \frac{1}{3} (T^{\frac{1}{2}} - T^{\frac{3}{2}}),
\end{aligned} \tag{4}$$

2 K_L -FACILITY

The neutral kaon beam (K_L) was simulated using bremsstrahlung photon beam scattered with beryllium target 24 m upstream of the LH_2/LD_2 cryogenic target. The main mechanism of K_L production is via ϕ -meson photoproduction, which yields the same number of K^0 and \bar{K}^0 . Based on the angular distribution calculated from ref [33], we see that the ϕ decay in its rest frame is mostly perpendicular to the axis of ϕ -momentum. Since K_L s need to stay along the original photon beam direction to get to the LH_2/LD_2 cryogenic target, this condition requires that the ϕ production and decay angles in the laboratory frame be about the same. That means that we will have only K_L s from ϕ -mesons produced at relatively high momentum transfer t at the Be target. The simulated momentum distribution for K_L is shown in Figure 2. Table 1 shows the beam condition for electron, photon and kaon at the K_L experiment.

Table 1: Expected electron/photon/kaon beam conditions at the K_L experiment.

Property	Value
Electron beam current (μA)	5
Electron flux at CPS (s^{-1})	3.1×10^{13}
Photon flux at Be-target $E_\gamma > 1500$ MeV (s^{-1})	4.7×10^{12}
K_L beam flux at cryogenic target (s^{-1})	1×10^4
K_L beam σ_p/p @ 1 GeV/c (%)	~ 1.5
K_L beam σ_p/p @ 2 GeV/c (%)	~ 5
K_L beam nonuniformity (%)	< 2
K_L beam divergence ($^\circ$)	< 0.15
Background neutron flux at cryogenic target (s^{-1})	6.6×10^5
Background γ flux at cryogenic target (s^{-1}), $E_\gamma > 100$ MeV	6.5×10^5

Schematic view of the Hall D beamline for the KLF is presented in top panel of Figure 3. Detail description of it is presenting in the proposal. Bottom panel of Figure 3 is the GlueX detector. The GlueX detector is azimuthally symmetric and nearly hermetic for both charged particles and photons, and is shown in Fig. 3. The largest element of GlueX detector is solenoid magnet, providing a magnetic field of about 2 T along the direction of the beam. The K_L beam momentum and time resolution are governed by the time resolution provided by the GlueX detector from the reconstruction of charged particles produced in the LH_2/LD_2 target. There are three detector systems that can provide precision timing information for reconstructed charged particles in GlueX: the Start Counter (SC), Barrel Calorimeter (BCAL), and Time-of-Flight (TOF) detectors. The simulation studies perform

K_L beam profile

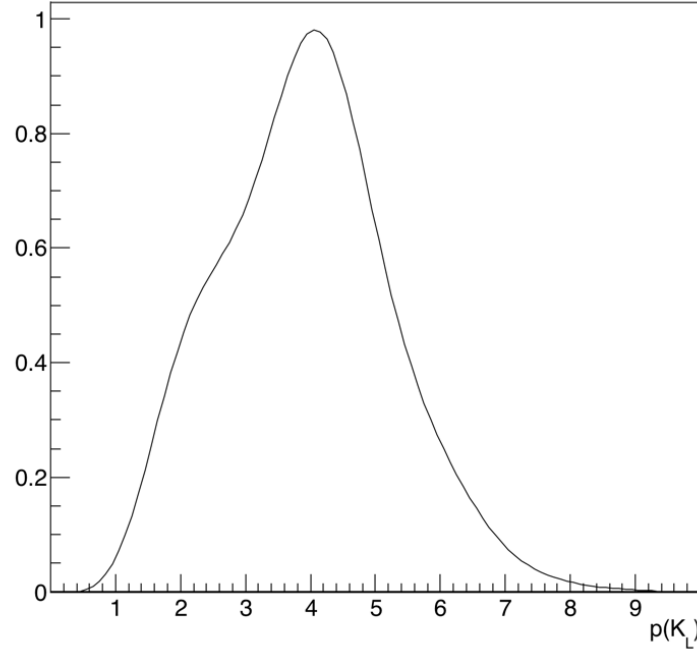


Figure 2: K_L momentum spectra originating from all sources at the Be-target. Total expected flux on GlueX target is $10^4 K_L/sec$.

here assumed a time resolution of 250 ps. More details on the detector components and their performance is described in Ref. [34].

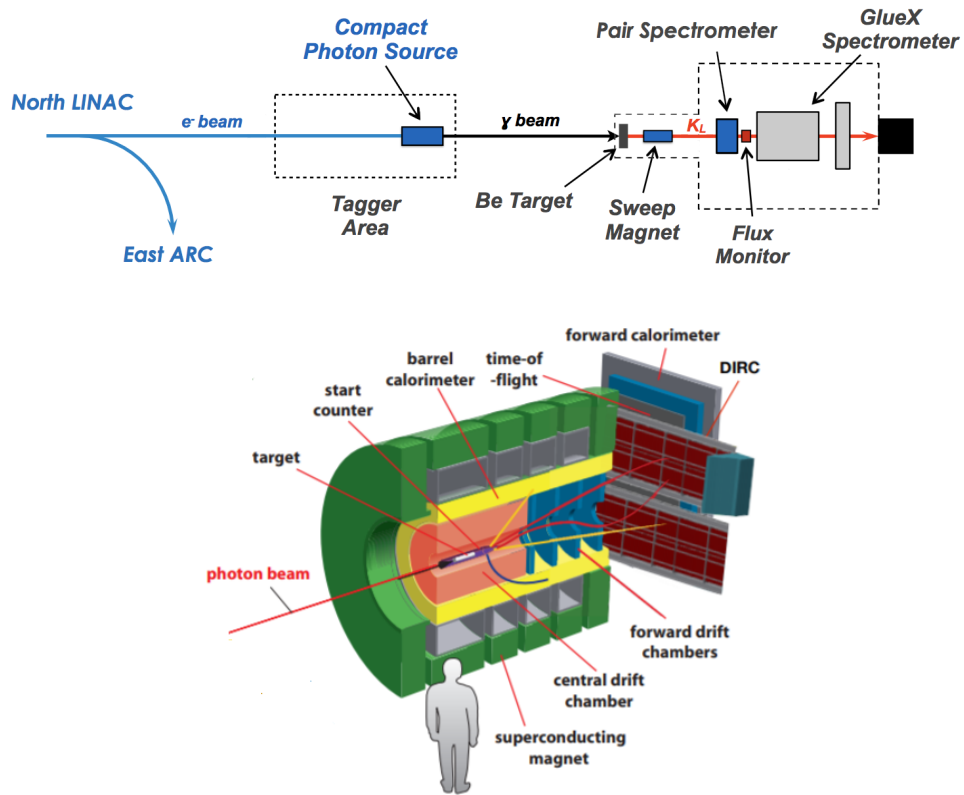


Figure 3: Top Panel: Schematic view of K_L -facility which contains Hall D beam line on the way $e \rightarrow \gamma \rightarrow K_L$, Compton Photon Source, the Be target, sweep magnet, and neutral kaons FM. Beam goes from left to right. Bottom panel: The GlueX spectrometer in Hall D at JLab.

3 PARTICLE IDENTIFICATION

For each channel, one primary particle (the K^+ for $K^+\pi^-p$, the K^- for $K^-\pi^0\Delta^{++}$, and the π^- for $K_L\pi^-\Delta^{++}$) provides a rough determination for the position of the primary vertex along the beamline that is used in conjunction with the SC to determine the flight time and path of the KL from the beryllium target to the hydrogen target, and thus determines its momentum. Protons, pions, and kaons are distinguished using a combination of $\frac{dE}{dx}$ in the chambers and Time-of-Fight to the outer detectors (BCAL and TOF). The energy loss and timing distributions for the $K^-\pi^0\Delta^{++}$ channel are shown as an example in Fig 4.

In Sec. 5, the photons from π^0 are reconstructed using the shower quality topology. The shower quality is defined a score between 0 and 1 to the neutral shower in FCAL using machine learning technique. The cut on shower quality removes the uncorrelated showers in FCAL that can be misidentified as photon in our analysis. The source of those showers mostly likely are the hadronic split-off of showers. We choose the quality score greater than 0.5.

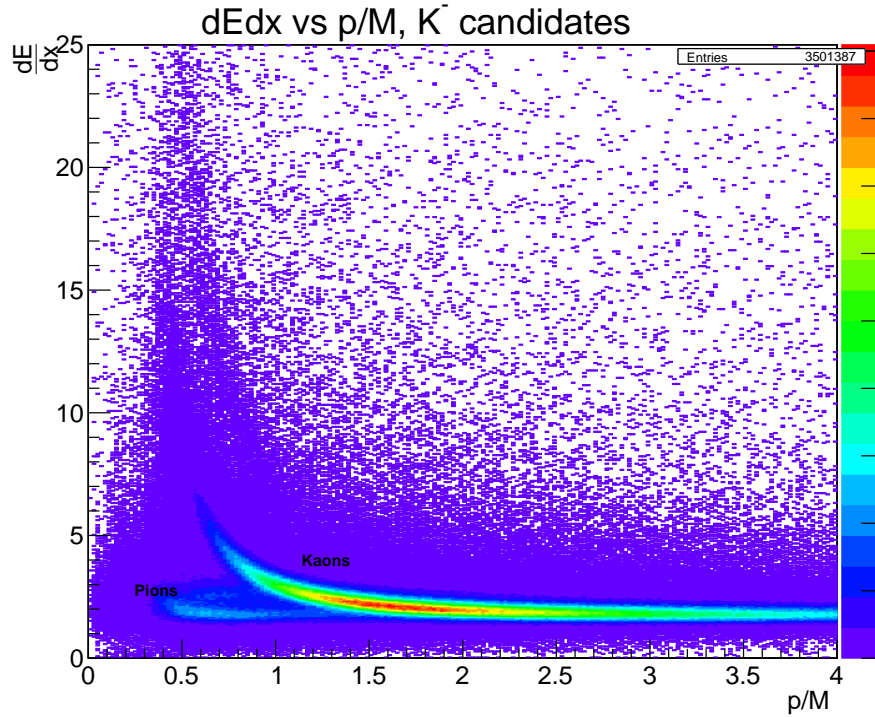


Figure 4: Particle Identification: dE/dx for $K^-\pi^0\Delta^{++}$

4 DETAILS OF MC STUDY FOR $K_L p \rightarrow K^\pm \pi^\mp p$

For this channel, a MC simulation is made to study the $K\pi$ P -wave in the proposed K_L facility. The model used for the MC generation is the Regge Model describing the neutral exchange production [35] with charged kaon beam, and we adapted for the neutral kaon beam. The theoretical model showed a good agreement with the data produced with beam momenta between 2.1 and 10 GeV/ c and four momentum transfer up to 1 GeV². In this simulation study, we assume that the neutral exchange with charged kaon beam is similar to neutral kaon beam.

The number of MC events generated in this study was 1 M event, weighted by the beam profile described in Sec. 2. A relativistic Breit-Wigner is used to simulate the $K^{*0}(892)$ resonance, and the kinematics of the decay daughters K^+ and π^- are simulated uniformly in the phase-space of $K^{*0} \rightarrow K^+\pi^-$. Figure 5 shows the generated $-t$ distribution and invariant mass of $K^+\pi^-$.

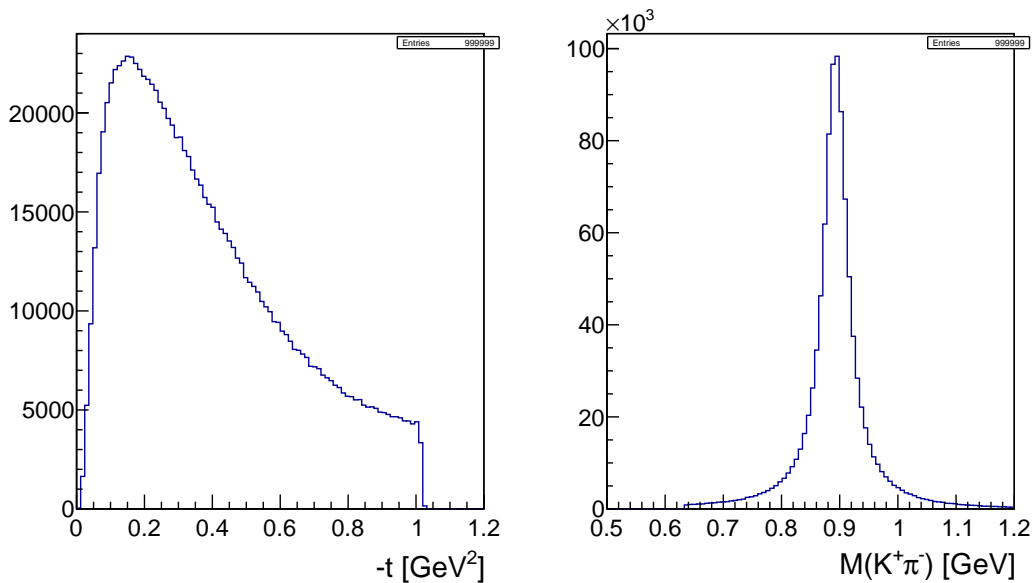


Figure 5: Generated MC distributions. Left: Four-momentum transfer $-t$. Right: $K^+\pi^-$ invariant mass.

Next, these generated events sample is simulated through GlueX detector using HDGeant package, which is the GlueX software developed by the GlueX Collaboration to simulate the detector response. Finally, the reconstruction of simulation is made by the JLab Reconstruction Framework JANA. The selection of the reconstructed MC events is performed using the

Particle Identification (PID) variables dE/dx , the deposit energy from the Central Drift Chamber (CDC) and Forward Drift Chamber (FDC) of GlueX spectrometer. In addition, the time difference from the Time-Of-Flight (TOF) was used to identify the forward pion and kaon in the final state. More details on particle identification is described in Section 3. The number of reconstructed and selected MC events are about 58 K events, which represents an integrated efficiency of the reconstruction and selection equal to 5.9%. Fig. 6 shows the reconstructed/selected MC events integrated over the entire range of beam momentum.

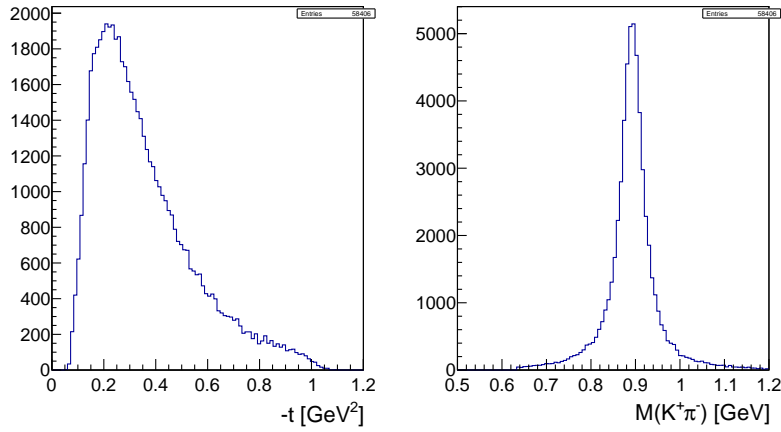


Figure 6: Reconstructed MC distributions. Left: $-t$ variable. Right: Invariant mass of $K\pi$ system, $M(K^+\pi^-)$.

We have performed a dedicated resolution and efficiency study to quantify the improvement that KLF facility can provide. The Fig. 7 (left) represents the relative resolution of the negative four momentum transfer $-t$ and the $K\pi$ invariant mass $m_{K^+\pi^-}$ (right). The invariant mass resolution is less than 1.2% over the full range of interest.

The reconstruction and selection efficiencies for the variables $-t$ and $m_{K\pi}$ are shown in the figure 8. For $-t$ variable, the efficiency varies from 0 to 10%. But for $m_{K\pi}$, the efficiency seems more or less consistent, and with averages around 6%. The efficiency for $-t$ goes zero for $-t$ less than 0.08 GeV^2 because of poor reconstruction of recoil proton. After repeating the same analysis without detecting the proton in final state, $K_L p \rightarrow K^+\pi^-(p)$, the reconstruction efficiency is quite high even at very small $-t$ bin of 0.02 GeV^2 and is shown in Figure 9. For the same analysis, the Fig. 7 (left) shows the relative resolution of the negative four momentum transfer $-t$ and the $K\pi$ invariant mass $m_{K^+\pi^-}$ (right). Without detecting proton and with this resolution of $-t$, we could study the $K\pi$ production mechanism with better statistics at small $-t$.

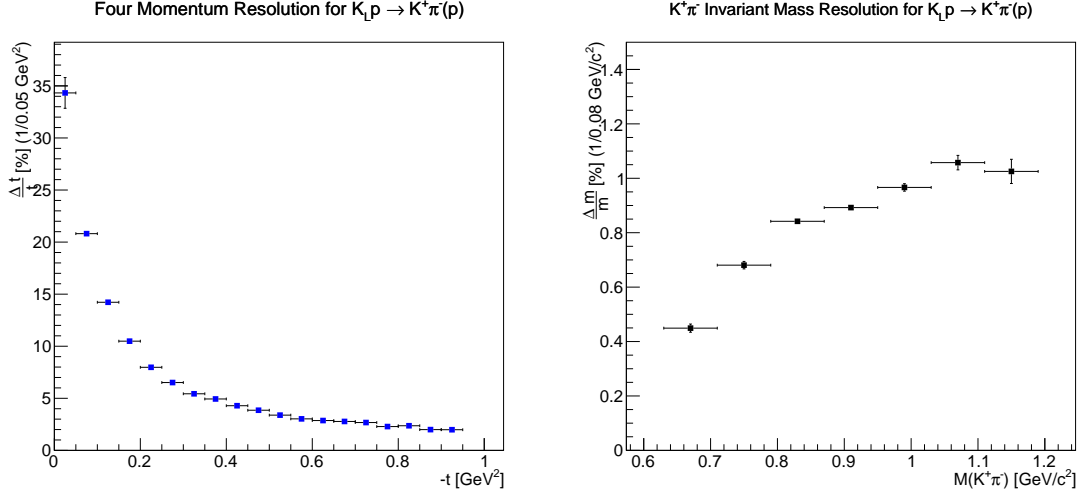


Figure 7: For missing proton analysis in $K_L p \rightarrow K^+ \pi^-(p)$. Left: Four momentum transfer relative resolution (σ_t/t) as a function of $-t$. Right: Invariant mass relative resolution (σ_m/m) as a function of $M(K\pi)$.

The Fig. 10 show the missing mass for $K_L p \rightarrow K^+ \pi^- X$, and is peaking at the rest mass of proton. Different panels in the figure refer to the missing mass distribution for different beam momentum. The beam was measured using the TOF detector. So, the resolution of missing mass ($MM(K^+ \pi^-)$) is driven by the TOF timing resolution, *i.e.*, 150 ps.

4.1 $K^*(892)$ Production in KLF

Knowing the total acceptance with the cross section and expected luminosity we can estimate the expected number of events of the $K^{*0}(892)$ production in KLF. Almost 50 % of the neutral $K\pi$ P -wave are produced as $K_L p \rightarrow K^{*0}(892)(K^+ \pi^-)p$ and the rest as $K_L p \rightarrow K^{*0}(892)(K^- \pi^+)p$. Assuming that the reconstruction and selection efficiency of the final state $K^+ \pi^- p$ is the same as $K^- \pi^+ p$, we can estimate the total number of events of the neutral K^* that can produced in KLF during for a given period of time. The expected number of events is estimated as follows,

$$N(\vec{p}) = \sigma_{K^*}(\vec{p}) \times BR(K^* \rightarrow K^+ \pi^-) \times \int \mathcal{L} dt \times \epsilon_{tot}(\vec{p}) \quad (5)$$

where \vec{p} is the beam momentum, σ is the total cross section of K^* production, $BR K^*(892) \rightarrow K^+ \pi^-$ is the branching ratio (≈ 100 %). $\epsilon_{tot}(\vec{p})$ is the total efficiency function of beam

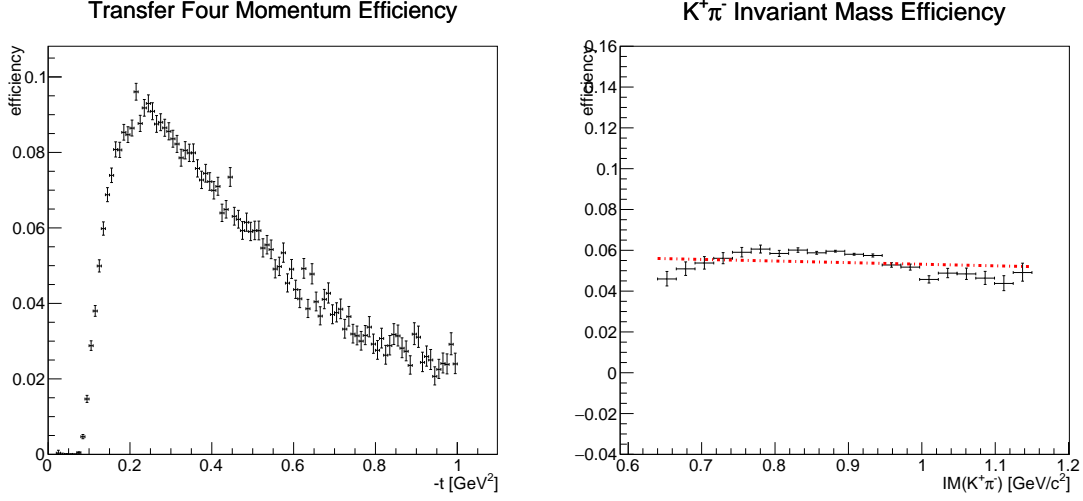


Figure 8: Reconstruction and selection efficiency of four momentum transfer (left) and $K^+\pi^-$ invariant mass (right) from the analysis of proton detected in final state.

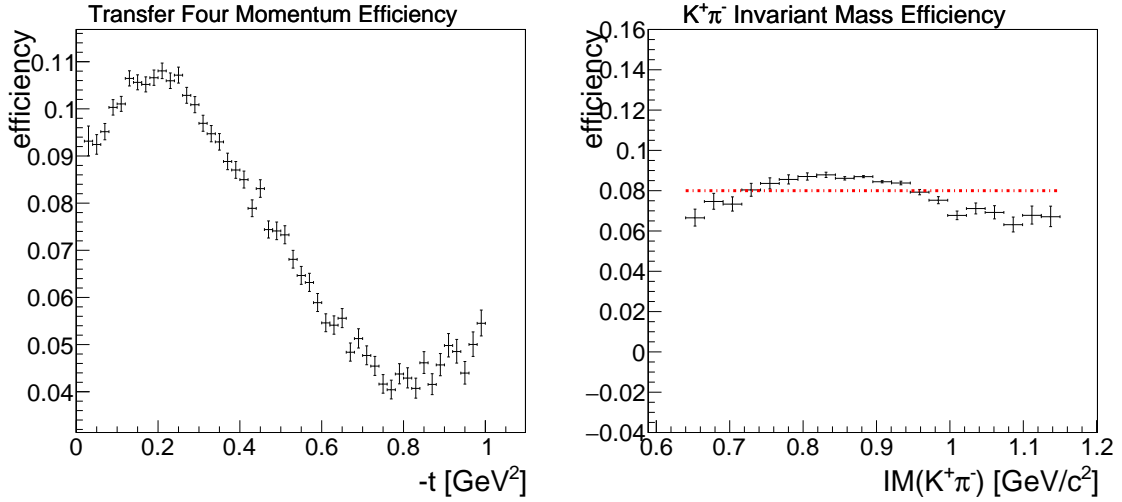


Figure 9: Reconstruction and selection efficiency of four momentum transfer (left) and $K^+\pi^-$ invariant mass (right) from the analysis of missing proton in the final state.

momentum and $\int \mathcal{L} dt$ is the integrated luminosity over the time, and is given as,

$$\int \mathcal{L} dt = n_K n_t T, \quad (6)$$

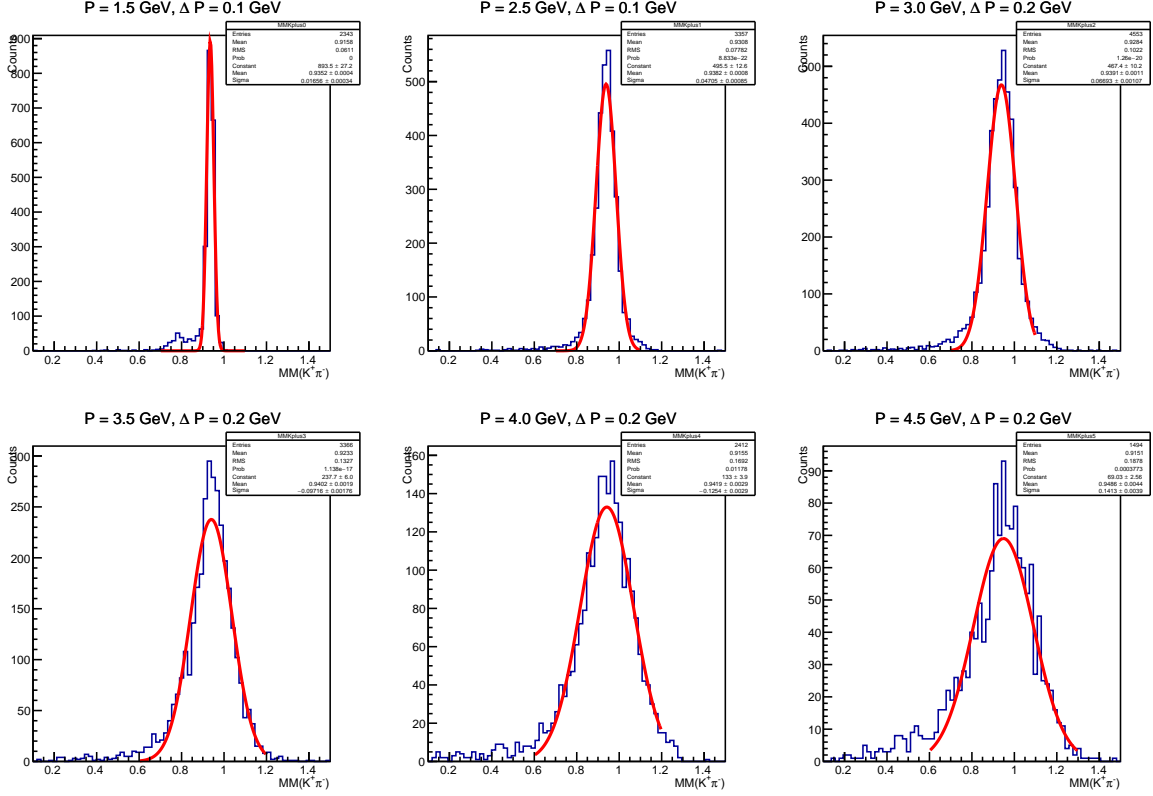


Figure 10: Different panels show the missing mass for $K_L p \rightarrow K^+ \pi^- X$ in different beam momentum. It is then fitted by the Gaussian distribution.

where n_K is the rate of incident K_L on target per second, n_t is the number of scattering centers per unit area and T is the integrated live time of the detector.

In Figure 11, we are comparing total statistics from KLF of 100 days running with previous high statistics experimental data, *i.e.*, SLAC. We expect one to two orders of more statistics for different $-t$ bins in K^{*0} production. In addition, the missing proton analysis will have smaller $-t$ coverage compare to the detected proton analysis.

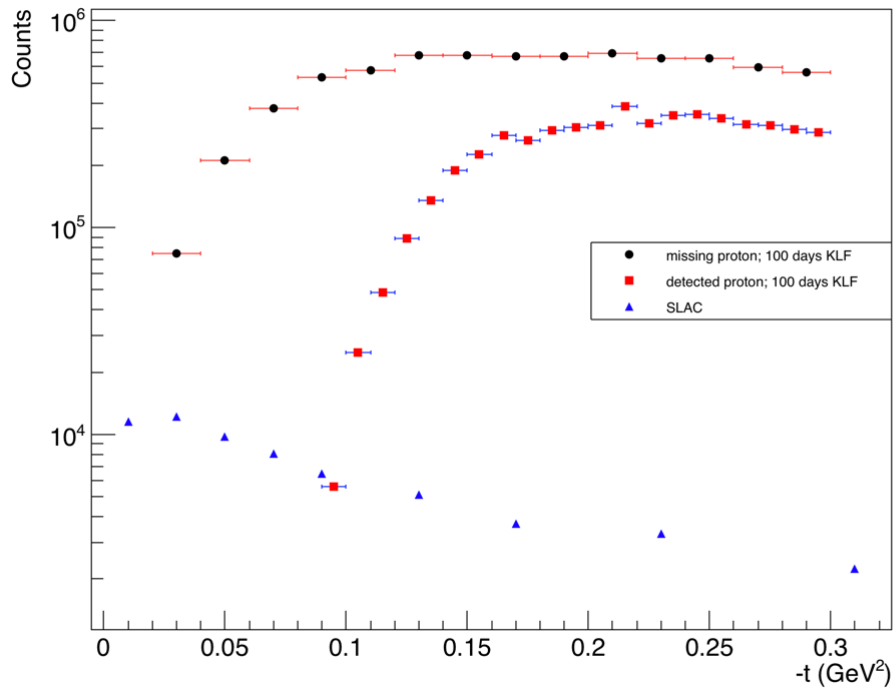


Figure 11: Statistics comparison between 100 days KLF production of $K^{*0}p$ for missing and detected proton in final state and SLAC data from Ref. [38]

5 DETAILS OF MC STUDY FOR $K_L p \rightarrow K^- \pi^0 \Delta^{++}$

The reaction $K_L p \rightarrow K^- \pi^0 \Delta^{++}$ is simulated using the theoretical $K\pi$ scattering amplitude and phase provided by Rhodas [15]. More details is in Appendix A.1. Figure 13 shows a sample plot for polar angle versus momentum distribution of K^- , π^+ , proton and π^0 from the generated event (left) and reconstructed event (right). A generated P -wave is then weighted using relativistic Breit-Wigner $K^{*-}(892)$ resonance and is shown in Figure 13.

The phase space of recoil Δ^{++} depends on the kinematics of $K\pi$ system. Figure 14 shows generated Breit-Wigner shaped Δ -resonance with mass 1.232 GeV and variable width calculated using Eq. (7).

$$\Gamma(q) = \frac{0.74 \times q^3 \times 6.3^2}{(1 + 6.3^2 \times q^2)}, \quad (7)$$

where q is the decay pion momentum.

Events were processed through the standard Hall-D GEANT simulation with GlueX detector and momentum smearing and utilized JANA for particle reconstruction that was simulated. The particle identification of charged particles follow the similar approach presented in the previous Section and also in Sec. 3. In case of neutral particle, the π^0 was set to be decayed in the GEANT and is reconstructing using neutral identification described in Section 3. The reconstructed π^0 distribution is shown in Fig. 15. We applied 3σ invariant mass cut on π^0 to remove any possible background of photons. With this selection, the reconstructed invariant mass of $K^- \pi^0$ is shown in Fig. 15.

The $K\pi$ production mechanism is depend on the beam momentum and four momentum transfer. Previous SLAC studied for partial wave analysis [19] was conducted with charged kaon beam at 13 GeV for a single t' bin less than 0.15 or 0.2 GeV² for four different reactions. Here we have performed a dedicated efficiency and resolution study to quantify the improvement that KLF facility can provide. Figure 16 (left) represents the relative resolution of the negative four momentum transfer ($-t$) and the $K\pi$ invariant mass $m_{K-\pi^0}$ (right). The relative resolution of $-t$ is very high, varying between 3% to 6% above 0.3 GeV², whereas it is increasing towards threshold to 14%. This behaviour came from low momentum of particles, proton and pion decayed from the recoil delta. However, this resolution is sufficient to have a binning width of 0.02 GeV² at low $-t$ region. The Fig. 16 (right) show the invariant mass relative resolution σ_m/m varying from 4 to 9%. The invariant mass resolution is directly depend on the reconstruction of neutral kaon in the final state.

An efficiency study on the variables $p(K_L)$, t and $m_{K\pi}$ were made to evaluate the improvement on the study of the $K\pi$ system with KLF. According to this simulation, the total integrated efficiency for the reaction $K_L p \rightarrow K^- \pi^0 \Delta^{++}$ is found to be about 7% and this

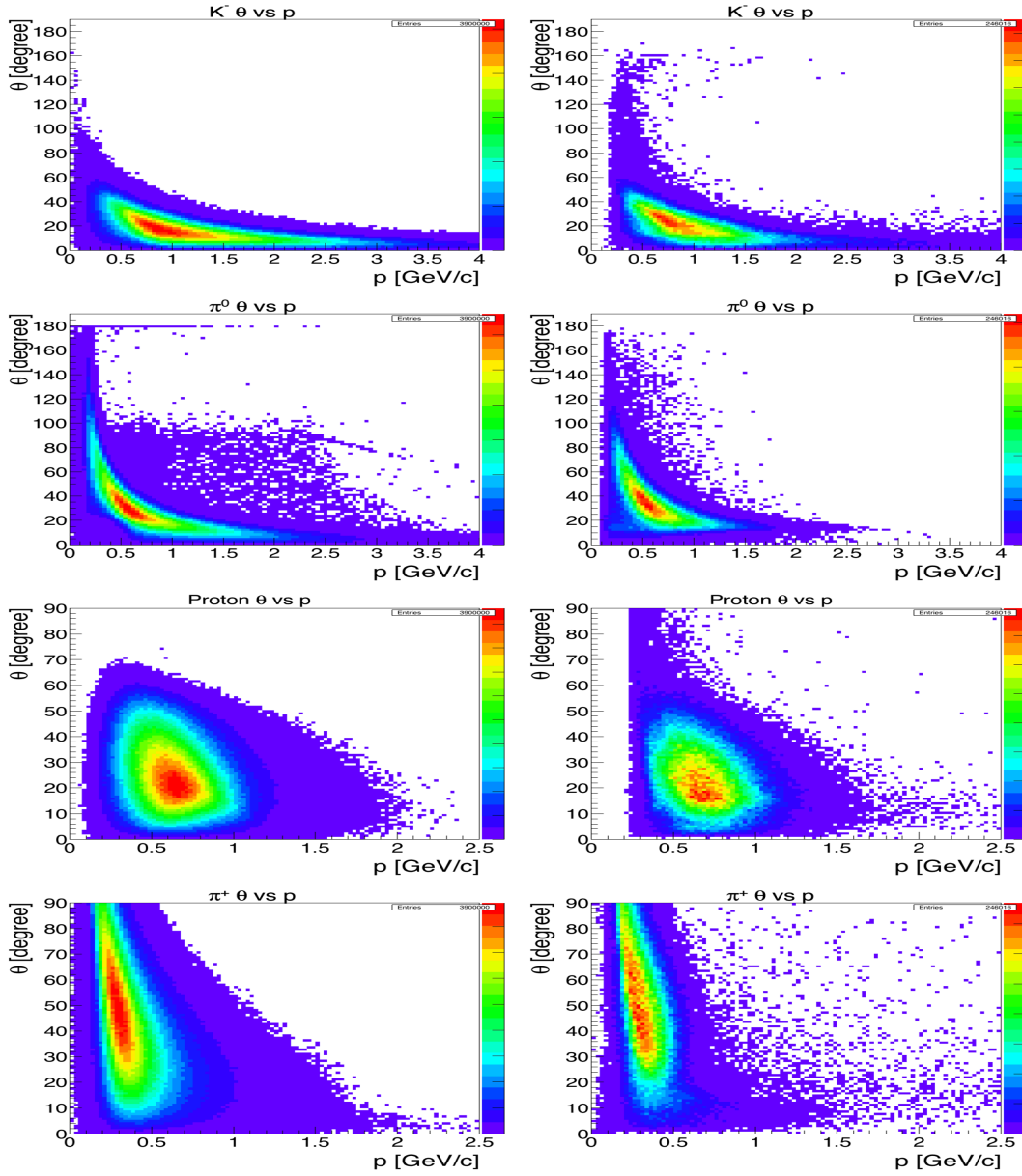


Figure 12: Momentum and angular distribution for the different particles. First row panel: K^- , Second row panel: π^0 , Third row panel: Proton, and Fourth row panel: π^+ . In each row panel, the first column is for generated distribution and the second column is for reconstructed distribution.

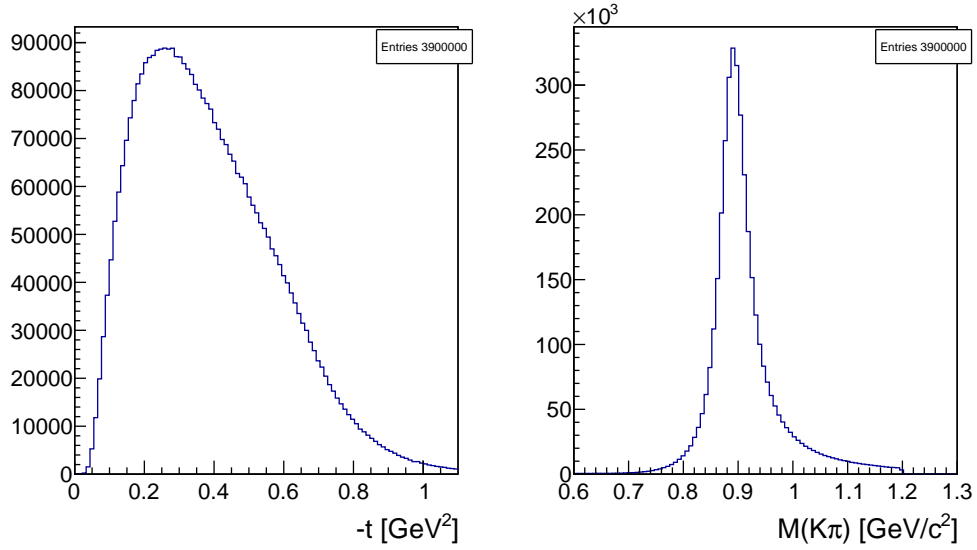


Figure 13: Generated kinematics of momentum transfer $-t$ (left) and K^* mass (right).

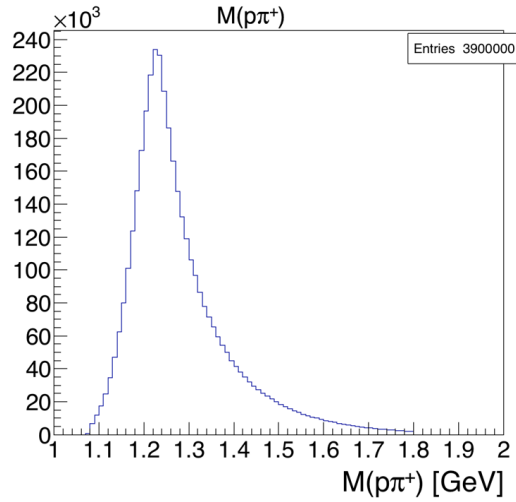


Figure 14: Generated Breit-Wigner shaped Δ -resonance of mass $M = 1.232$ GeV and width from Eq. (7).

value remains uniform almost all bins of $-t$. Also, the efficiency of $K^-\pi^0$ invariant mass is uniform over the entire mass range, see Fig. 17. With this efficiency and the beam flux, we

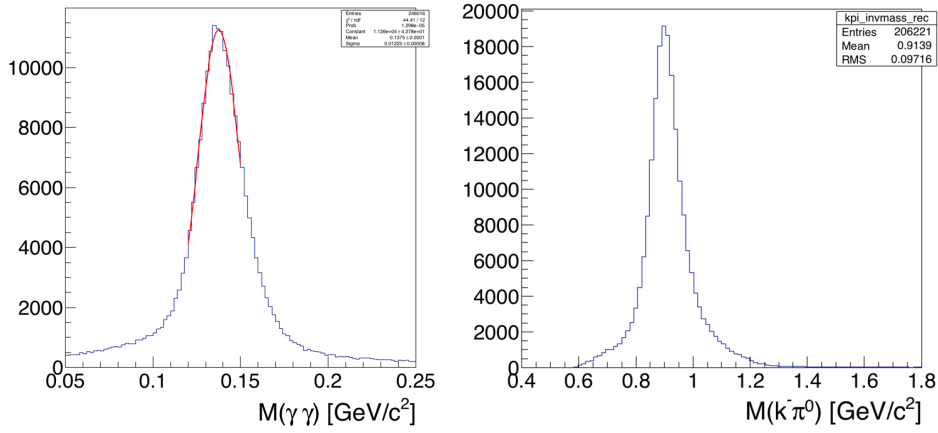


Figure 15: Left: Invariant mass of two photons peaked at π^0 mass. Right: Invariant mass of $K^-\pi^0$.

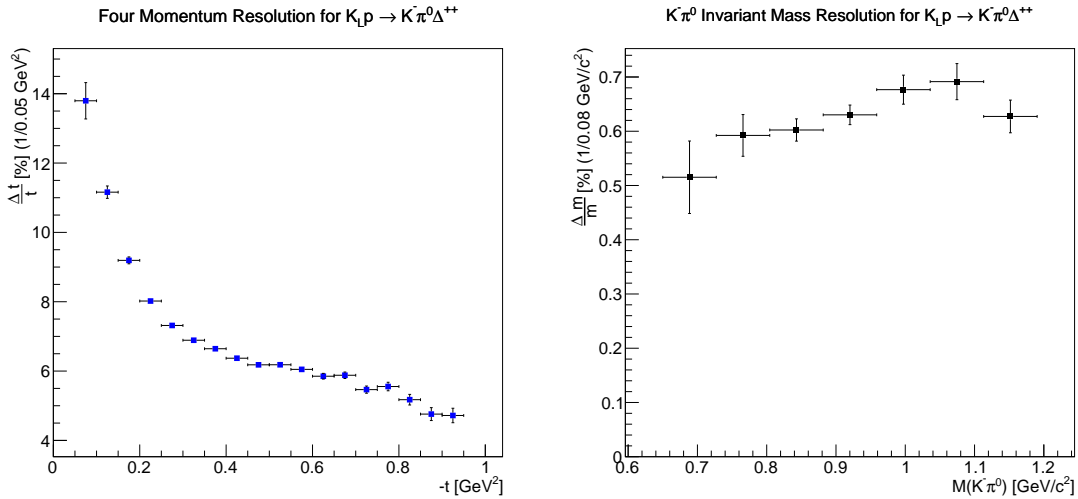


Figure 16: Left: Four momentum transfer relative resolution (σ_t/t) as a function of $-t$. Right: Invariant mass relative resolution (σ_m/m) as a function of $M_{K\pi}$.

estimated the expected number of K^* for 100 days of KLF running for $-t < 0.2 \text{ GeV}^2$ and is shown in Fig. 18.

The $K\pi$ S -wave was also simulated below 1.2 GeV using the dispersive parametrization described in Appendix A.1. The S and P wave simulation of the reaction $K_L p \rightarrow K^-\pi^0\Delta^{++}$

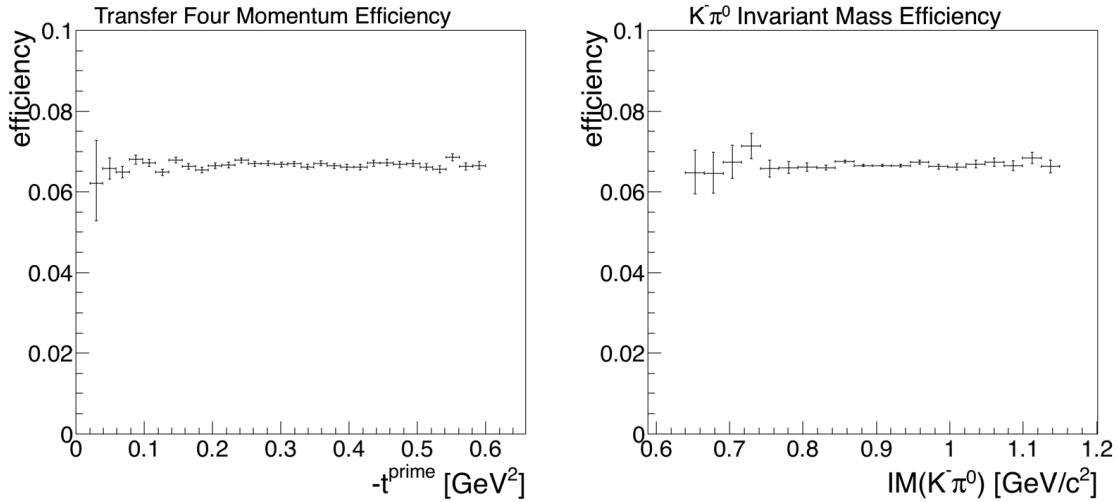


Figure 17: Efficiency of reconstruction of four-momentum transfer (left) and $K^-\pi^0$ invariant mass (right).

is used to estimate the total production in KLF after 100 days of running. We expect roughly 0.65M events for S -wave and 1.3M events for P -wave. Fig. 18 show 100 days expected statistics in KLF for S -wave (light blue) and P -wave (light red). On these data we are performing the partial wave analysis (more details in Sec. 7).

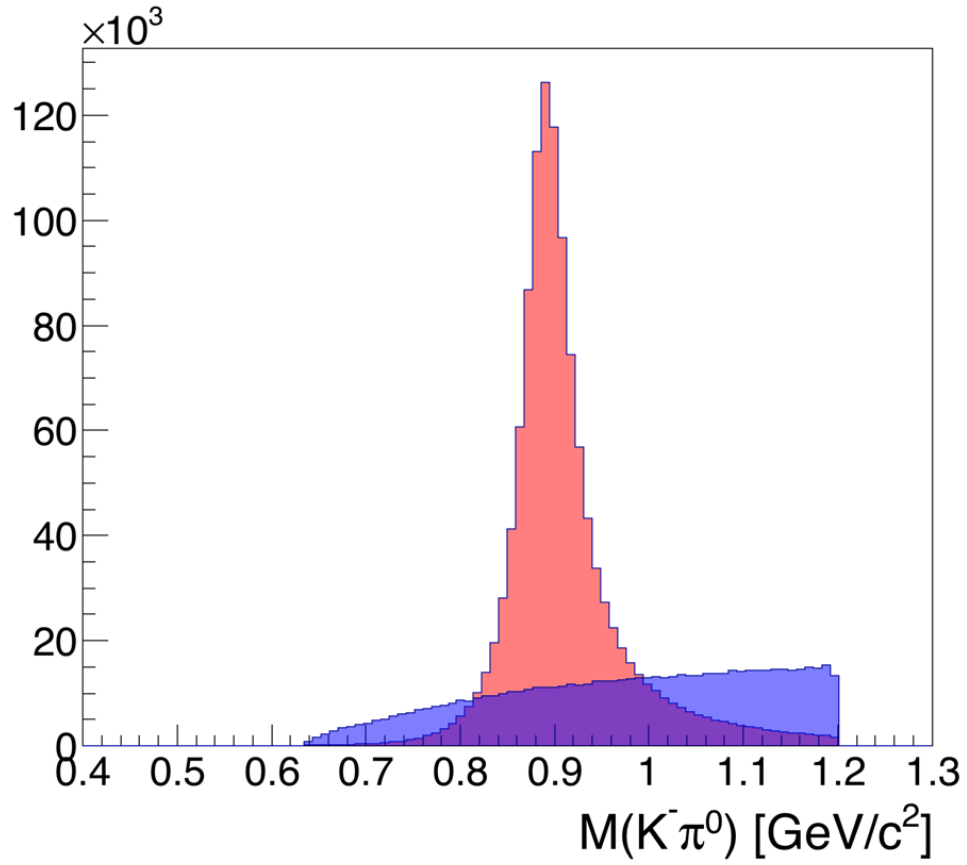


Figure 18: Expected distribution of the $K^-\pi^0$ invariant mass below 1.2 GeV after 100 days of running. The light red distribution represents the $K^-\pi^0$ P -wave and light blue distribution represents the S -wave.

6 DETAILS OF MC STUDY FOR $K_L p \rightarrow K_L \pi^- \Delta^{++}$

This Section described the reconstruction of $K_L p \rightarrow K_L \pi^- \Delta^{++}$ where particle identification and reconstruction is similar to previous channels. One main difference here is missing neutral kaon in the final state, K_L . From the missing mass technique, the neutral kaon is reconstructed. The resolution of missing mass $MM(p\pi^+\pi^-)$ is driven by the SC time resolution where the beam is determined from time-of-flight method, utilizing the 24 m flight path between the Be-target and the hydrogen target. Figure 20 shows W resolution ranges between 2 to 12%. This resolution could be improved by applying the constrained kinematical fit as described in hyperon analysis note [37]. Figure 21 shows an example of the invariant mass of $K\pi$ for generated (left) and reconstructed (right) events. Among those the top panel is for S -wave and bottom panel is for P -wave. For the final selection of the reaction $K_L p \rightarrow K_L \pi^- \Delta^{++}$, we have 3σ cut on missing mass distribution shown in Figure 20.

W Resolution for $K_L p \rightarrow K_L \pi^- \Delta^{++}$

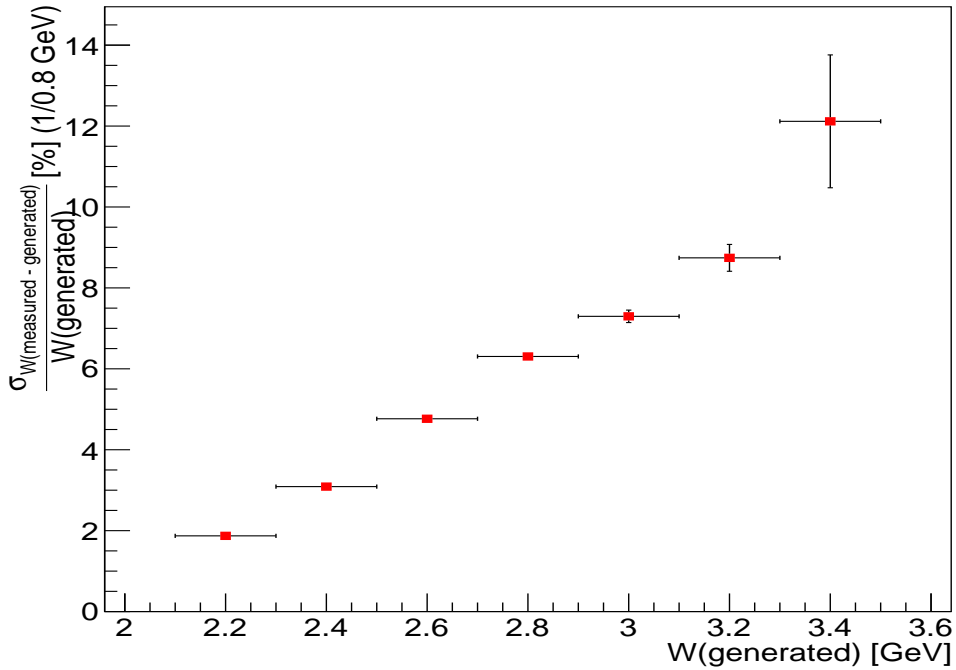


Figure 19: W -resolution for the $K_L \pi^- \Delta^{++}$.

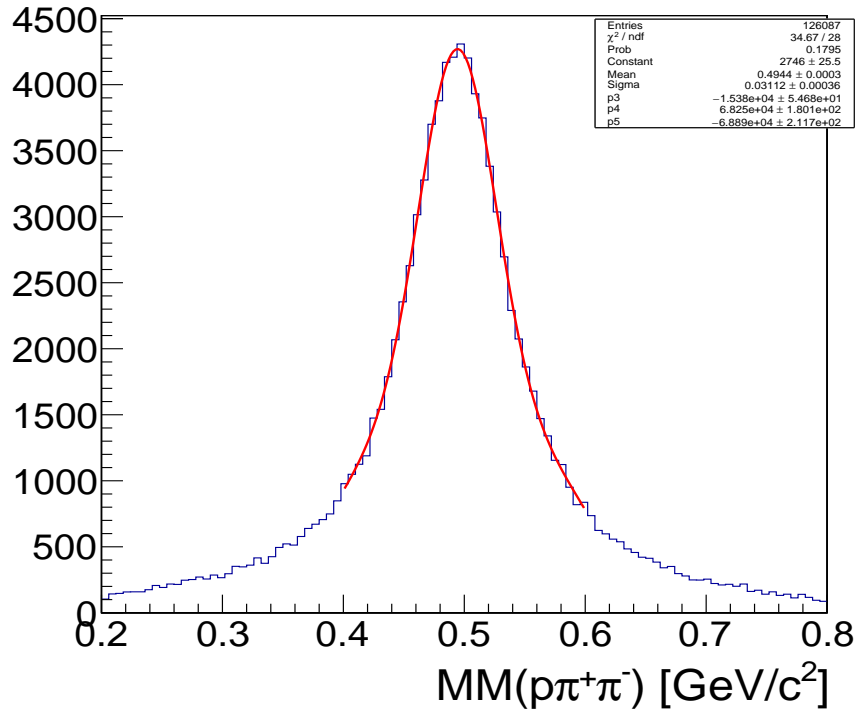


Figure 20: Fitted distribution for the missing mass from the reaction $K_L p \rightarrow \pi^- \Delta^{++} (p\pi^+) X$.

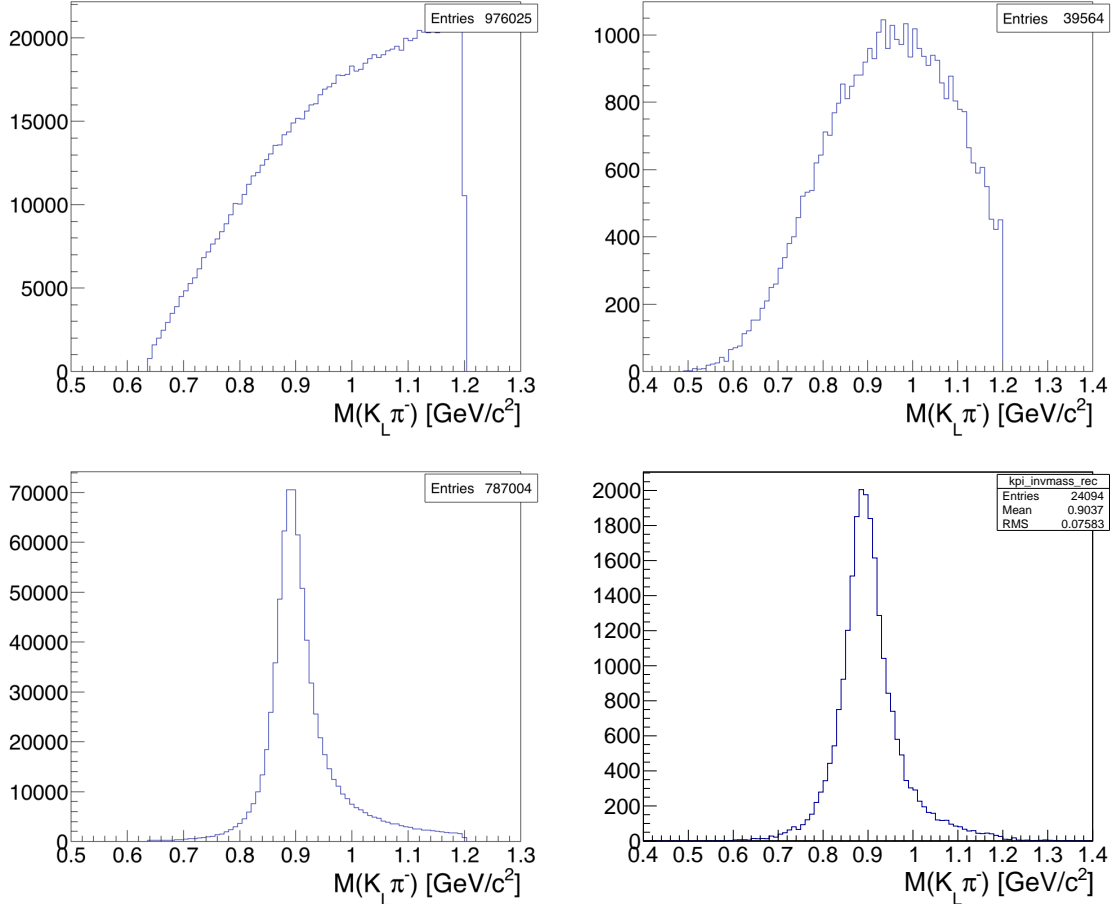


Figure 21: Generated and Reconstructed invariant mass of $K_L \pi^-$ for S - and P -wave. Top panel: S -wave generated (left) and reconstructed (right). Bottom panel: P -wave generated (left) and reconstructed with kinematic fitting (right), respectively.

Similar to previous analyses we have performed the efficiency and resolution studies. Figure 16 (left) represents the relative resolution of the negative four momentum transfer ($-t$) and the relative resolution of $K\pi$ invariant mass $m_{K^L \pi^-}$ (right). The $-t$ resolution is very high, varying between 3% to 6% above 0.3 GeV^2 , whereas it is increasing towards threshold to 13%. The invariant mass relative resolution (σ_m/m) is varying from 4 to 9%. The invariant mass resolution is directly depend on the reconstruction of neutral kaon in the final state.

In next Section, we will explain in detail the partial wave analysis and their results for

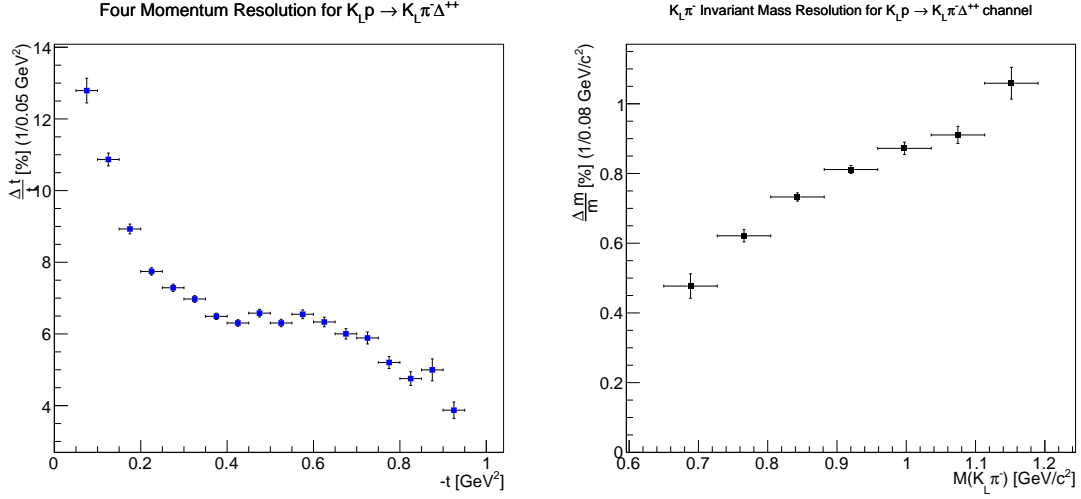


Figure 22: Left: Four-momentum transfer resolution. Right: Invariant mass $M(K_L \pi^-)$ resolution.

$K\pi \rightarrow K\pi$ elastic scattering. To isolate $K\pi$ elastic scattering from what we measure of $K_L p \rightarrow K_L \pi^- \Delta^{++}$, we are selecting events at small values of $-t$ (< 0.2 GeV²). The Fig. 23 shows reconstructed $-t$ as a function of beam energy. In particular at small values of $-t$, the pion exchange is more likely in the t -channel production compare to other processes. In this region of $-t$, we have almost similar statistics for this analysis as of previous channel (see Fig. 18). Even though the minimum momentum of recoil Δ is higher compare to proton (for the same value of $K\pi$ mass and beam energy), we have sufficient statistics at small $-t$ region where the decay particles of delta carried sufficient momentum which results successfully reconstruction in GlueX detector.

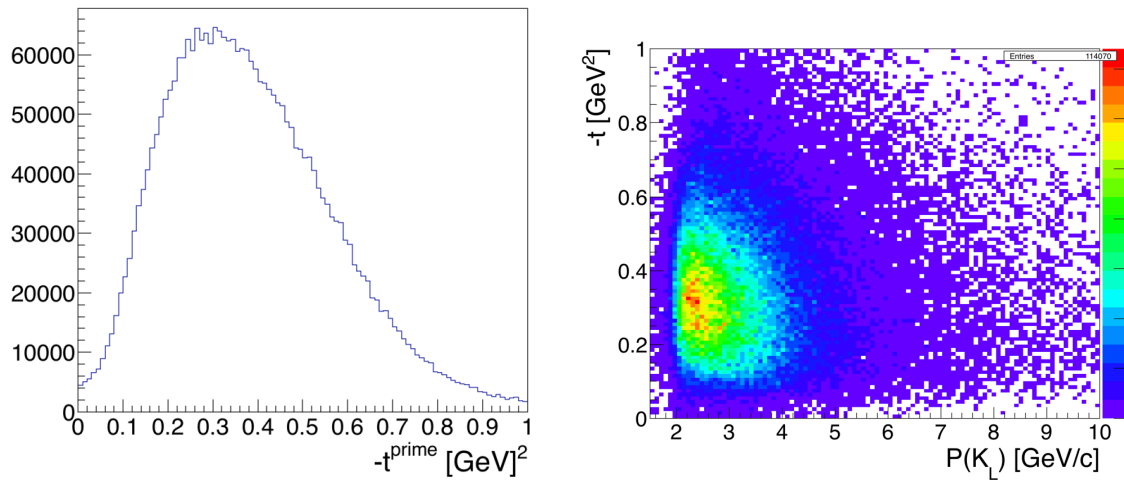


Figure 23: Left: Sample $-t'$ distribution. Right: Sample 2d distribution of $-t$ as a function of beam momentum.

7 PARTIAL WAVE ANALYSIS

Both nucleon and delta recoil reactions are used previously to calculate phase shift and amplitude for $K\pi$ scattering [19, 38]. In the small $|t|$ region, both nucleon and delta recoil channels are dominated by pion exchange. The π exchange contribution to the Δ recoil reactions does not vanish at $t = 0$ but it does in the nucleon recoil reactions. Although the behavior of the data as a function of t is very different for the nucleon and delta recoil reactions, there is a procedure developed by Estabrooks *et al.* [19] which enables us to calculate the $K\pi$ partial-wave amplitudes independent of the nature of the recoiling particles against the $K\pi$ system.

It is important to make clean sample of those reaction before conducting any partial wave analysis. Once this pion exchange portion has been isolated, an extrapolation to the pion pole ($t = \mu^2$) then yielded the real $k\pi$ elastic scattering amplitudes. In general, the data determines only the magnitude and relative phases of the amplitudes. An overall phase can not be determined. In the low mass region, $M(K\pi) < 1.2 \text{ GeV}$, the S - and P -waves are known to be elastic so that the imposition of elastic unitarity is sufficient to fix the overall phase.

From above analyses, we have two sets of reactions, neutral exchange $K_L p \rightarrow K^\pm \pi^\mp p$ and charge exchange $K_L p \rightarrow K^- \pi^0 \Delta^{++}$ or $K_L p \rightarrow K_L \pi^- \Delta^{++}$. The $K\pi$ scattering amplitude in final state is composed of two isospin components $1/2$ and $3/2$ with Clebsch–Gordan coefficients as,

$$K_L p \rightarrow K^+ \pi^- p = \langle K_L \pi^0 | K^+ \pi^- \rangle = \frac{1}{3}(T^{\frac{1}{2}} - T^{\frac{3}{2}}), \quad (8)$$

$$K_L p \rightarrow K^- \pi^+ p = \langle K_L \pi^0 | K^- \pi^+ \rangle = -\frac{1}{3}(T^{\frac{1}{2}} - T^{\frac{3}{2}}), \quad (9)$$

$$K_L p \rightarrow K^- \pi^0 \Delta^{++} = \langle K_L \pi^- | K^- \pi^0 \rangle = \frac{1}{3}(T^{\frac{1}{2}} - T^{\frac{3}{2}}), \quad (10)$$

$$K_L p \rightarrow K_L \pi^- \Delta^{++} = \langle K_L \pi^- | K_L \pi^- \rangle = \frac{1}{3}(T^{\frac{1}{2}} + 2T^{\frac{3}{2}}), \quad (11)$$

where T 's are the isospin components for $I = 1/2$ and $I = 3/2$. For S -wave scattering, both components are significant below 2 GeV. The $I=3/2$ S -wave is elastic and repulsive up to 1.7 GeV and contains no known resonances whereas $I = 1/2$ S -wave has a broad resonance peaking above 1350 MeV, is known as $K^*(1430)$. Beside that there are several phenomenological and experimental studies suggest a possible S -wave resonance with a very large width in the region close to the $K\pi$ threshold called κ (kappa), or $K_0^*(800)$. Because of limited experimental data for S -waves, both states are not well defined. For P -wave

scattering, the $I = 3/2$ is almost negligible below 2 GeV. But for $I = 1/2$, P -wave has two resonance one at 892 MeV, known as $K^*(892)$ and the second is the $K_1^*(1410)$ that exists above 1 GeV, although its properties are less precisely known.

For the reactions neutral kaon scattering off proton producing a $K\pi$ system with charged exchange, *i.e.*, reactions 8 and 9, due to elastic unitarity below 1.2 GeV, the P -wave ($3/2$) is almost zero. The overall phase of P -wave ($1/2$) for $t' < 0.2\text{GeV}^2$ is shown in Figure 24.

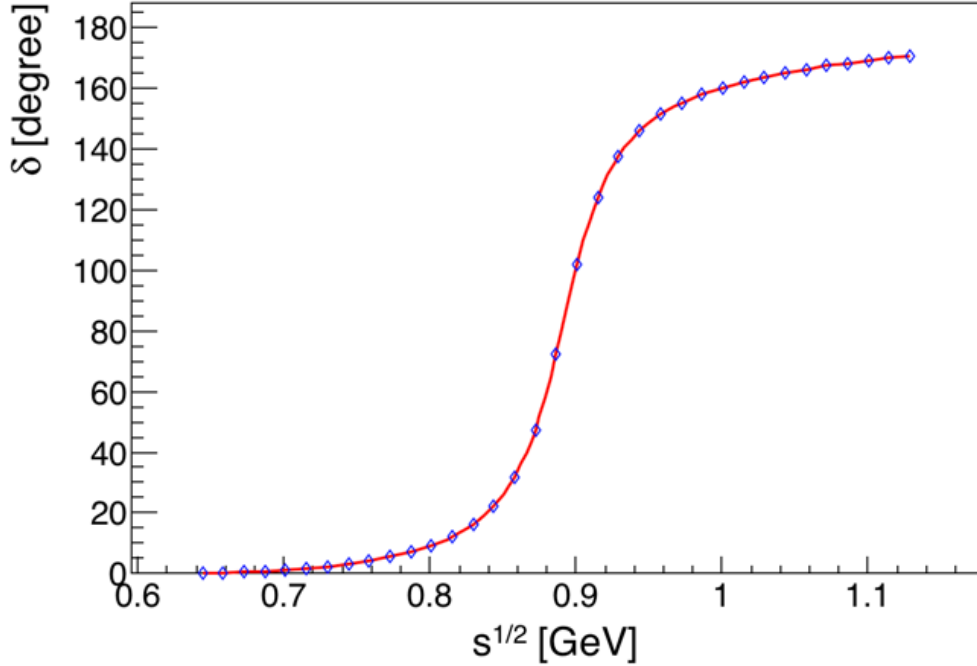


Figure 24: Phase-shift of P -wave $I = 1/2$. Expected KLF production 100 days of running that are generated using the parametrization of dispersive approach. Statistical errors are within symbols. Overall systematic uncertainties of 5% are not included.

For S -wave as mentioned above, there is most likely one resonance 0^+ exist around threshold mass of $K\pi$ with isospin $1/2$. In case of charged exchange reaction (such as Eqs. (8) and (9)) with neutral kaon beam, the S -wave final state is composed the two isospin components. Since the MC were produced using parametrization of dispersive approach as explained in Appendix A.1, the pure S -wave separation was carried from independent analysis of two reactions (Sec. 5 and Sec. 6). It should be noted that this separation was not performed for LASS. Actually, the existing $I = 3/2$ data are previous to LASS and of much

less precision, which is a large source of uncertainty that contaminates the extraction of the $I = 1/2$ amplitude and the κ or other strange resonance poles. On Figure 25, the upper panel shows the S -wave for $I = 1/2$, whereas the lower one shows the phase for $I=3/2$.

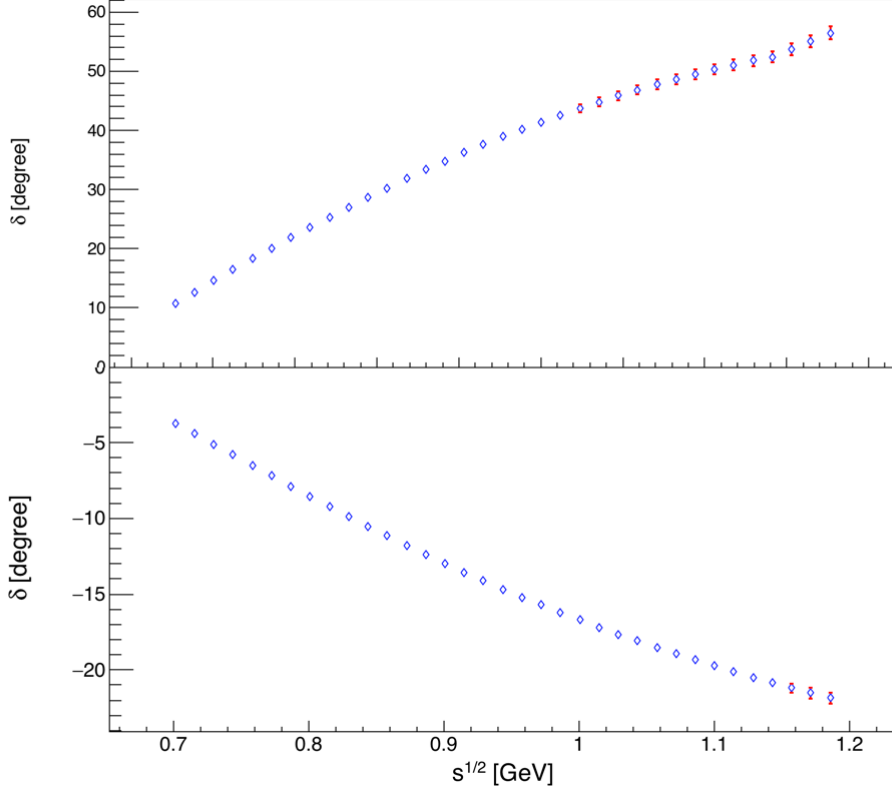


Figure 25: Top panel: S -wave phase-shift for isospin $I = 1/2$ and Bottom panel: isospin $I = 3/2$ as a function of \sqrt{s} , invariant mass of $K\pi$ system (see text for details).

In Fig. 26, the upper plot is phase shift for S -wave $I = 1/2$ which includes experimental data from SLAC. And the lower plot is phase shift for S -wave $I = 3/2$ with all available world data. The yellow band corresponds to the uncertainty of the fit to data without KLF, whereas the red diamond points are KLF expected result with statistical and systematic uncertainties added in quadrature. Since the MC generation used the parametrization from current dispersive relation study by Peláez and Rodas [39], the central value on the diamond points are normalized according to their results.

Finally, these data are used to recalculate the κ pole using the Roy-Steiner dispersion

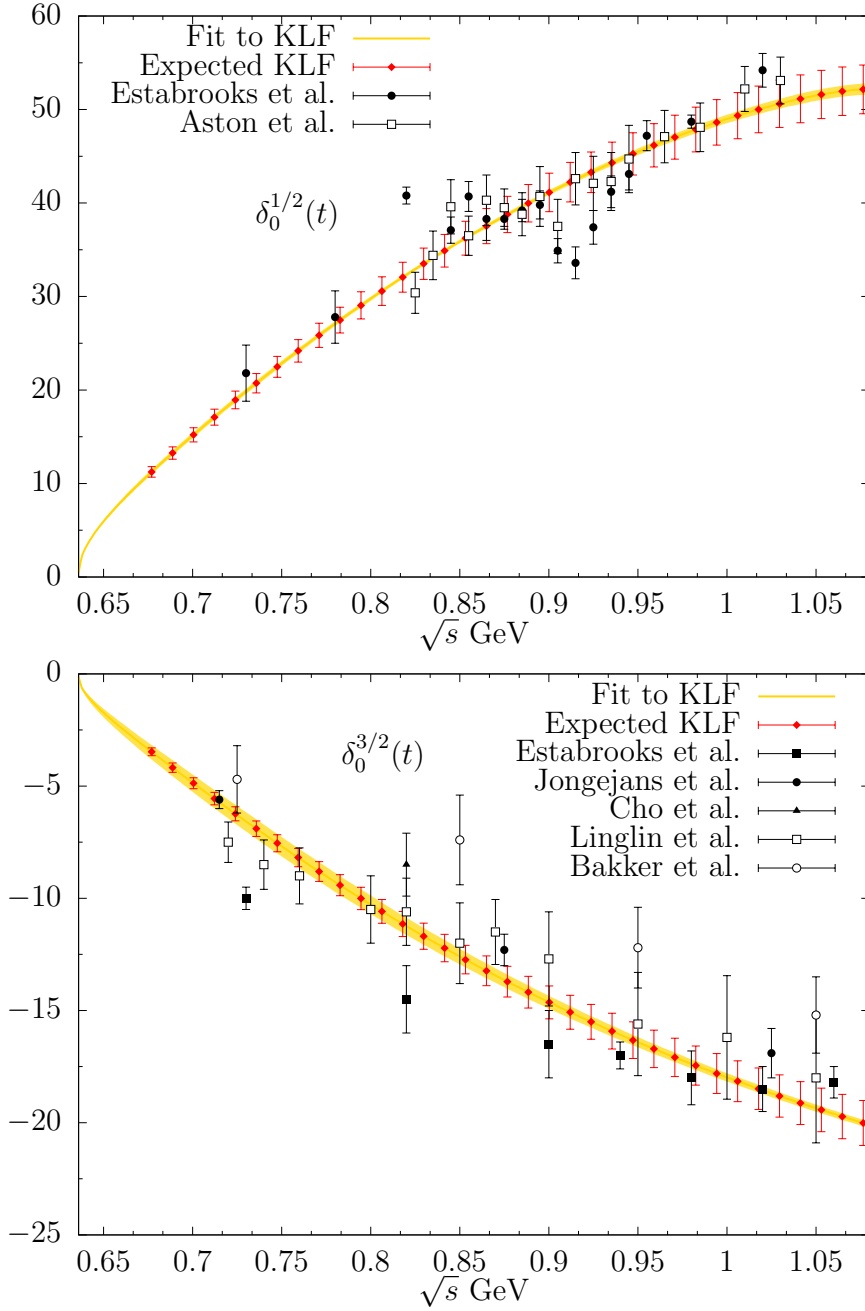


Figure 26: The S -wave phase-shift for isospin $I = 1/2$ (upper panel) and isospin $I = 3/2$ (lower panel). The fits were produced by Rhodas, author of Fig. 25. The KLF results include statistical and systematic errors from 100 days running of KLF.

dispersion relation. There are many *models* describing the $\kappa/K_0^*(700)$ and its associated pole (see the PDG2018 [44] for an exhaustive compilation). For illustration we show some representative results in Fig. 27. Note that many of them still use Breit-Wigner parameterizations, which unfortunately are not applicable in this case because they violate chiral symmetry and do not have the left and circular cuts that are numerically relevant for precise determinations of the $\kappa/K_0^*(700)$ pole. In spite of all these models, the Roy-Steiner Dispersion Relations provides the most rigorous determination of the $\kappa/K_0^*(700)$ pole with a realistic estimate of both statistical and systematic uncertainties. Thus, in order to estimate the effect of the proposed KLF experiment, we have recalculated the pole obtained by using a Roy-Steiner analysis either using all the existing data [41, 42, 43] or with the LASS data rescaled to the expected accuracy of the KLF experiment. In the first case, without KLF, Peláez *et al.* [41, 42] finds $M_\kappa \simeq 648 \pm 7$ MeV and $\Gamma_\kappa = 580 \pm 32$ MeV, whereas by using the expected KLF data the uncertainties are divided by slightly more than a factor of two for the mass, so that we find: $M_\kappa \simeq 648 \pm 4$ MeV; and by more than a factor of three for the width, finding: $\Gamma_\kappa = 580 \pm 16$ MeV. According to these results, just due to the precise KLF measurement, a significant improvement on the $\kappa/K_0^*(700)$ search can be performed, especially by improving the elastic region of the $K\pi$ invariant mass. Fig. 27 shows as pole positions in the complex plane, the different determinations of the κ mass and width, including the determination with the expected amplitude and phase-space that will be produced by KLF after 100 days of run. The expected result for the kappa pole is $\sqrt{s_\kappa} \equiv M - i\Gamma/2 = 648 \pm 4 - i 280 \pm 8$ MeV (the error coming from πK scattering is less than 1 MeV, the rest comes basically from the high energy Regge input and the crossed channel $\pi\pi \rightarrow K\bar{K}$ input to the dispersive integrals).

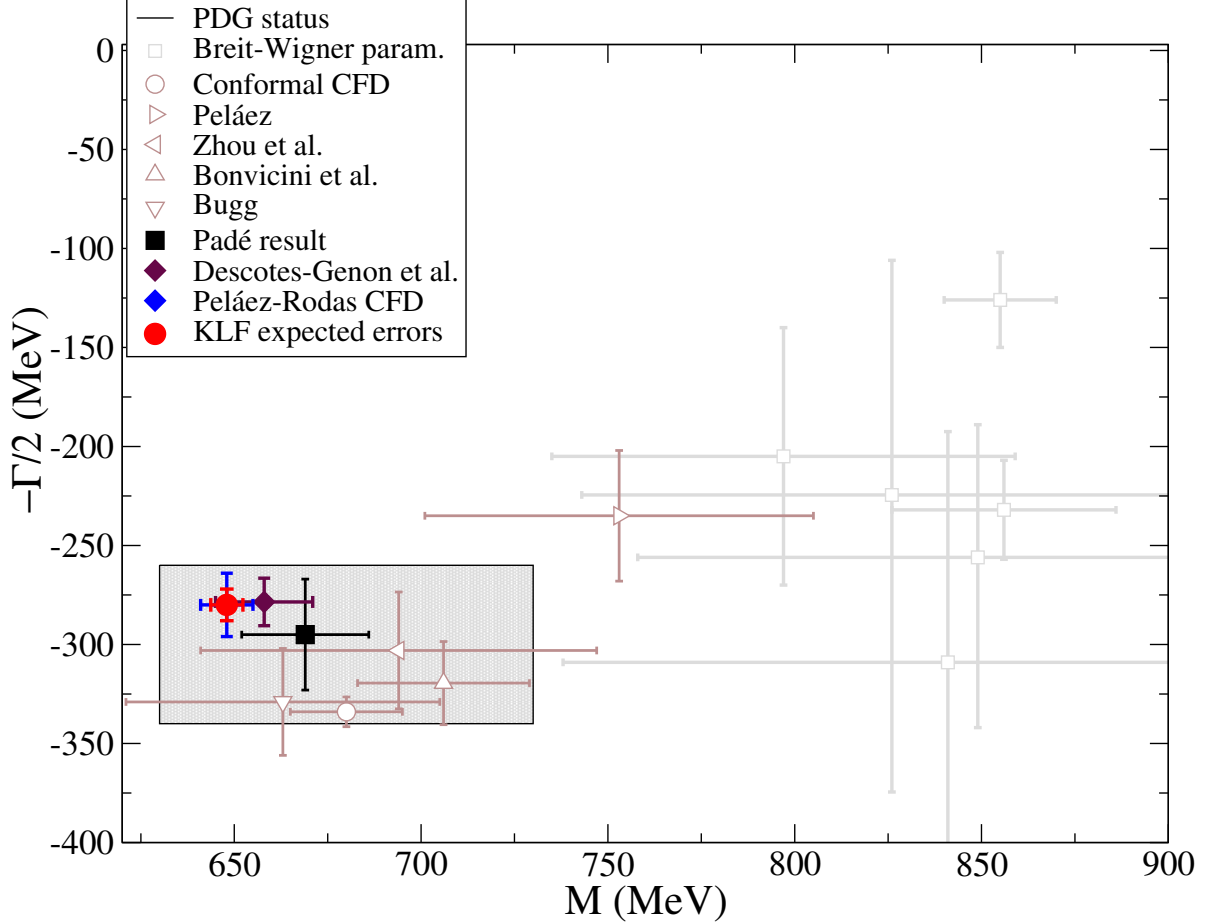


Figure 27: Present situation of the determinations of the $\kappa/K_0^*(700)$ pole. The figure is from Refs. [41, 42, 43] but we have added as a red point with uncertainties, the simulation of the pole position that would be obtained by means of a Roy-Steiner analysis by using simulated data from KLF experiment after 100 days of run, note that the blue error bars are for parameters obtained without KLF data and the tiny red error bar within blue are with KLF data. These calculations also include estimates of systematic effects. Note that the other points are either predictions [?] or illustrative models that may have additional systematic uncertainties due to their model dependence, like Breit-Wigner determinations. Shaded rectangle stands for PDG2018 uncertainties.

7.1 Partial wave analysis for neutral exchange

The other analyses we mentioned previously are the neutral exchange using K_L beam producing $K\pi$ by recoiling proton in final state. The study of this channel is presenting in details (Section 4) with two topologies, $K^+\pi^-p$ and $K^+\pi^-(p)$. For this channel the MC was produced including three partial wave S , P , and D . The structure caused by those waves can be seen directly in the scatter plot of fig. 29 from the reconstruction sample of $K_L p \rightarrow K^+\pi^-p$ channel, which show the cosine of the decay angle at $K\pi$ rest frame (Gottfried-Jackson) against $K^+\pi^-$ invariant mass for events with $t' < 0.2 \text{ GeV}^2$. Clear structure can be seen at $K^*(890)$ (P -wave) and $K_2^*(1430)$ (D -wave). Beside that there is distinct band at 1800 MeV which came from the interference of all three waves. With more production mechanism, the interference structure grows more complex at high masses. In any case, the complexity of those interference patterns demonstrate the importance of performing a partial wave analysis at the pion pole in order to fully understand the resonance structure. Previous measurement at SLAC perform partial wave analysis of $K\pi$ system from threshold to $2.6 \text{ GeV}/c^2$ including waves through H of $J^P = 5$. With limited waves and statistics in our MC sample, we are exercising the available tools and technique of partial wave analysis from GlueX that can be used in future KLF data analysis.

Here we are fitting three partial waves S , P , and D in the MC sample shown in Figure 29.

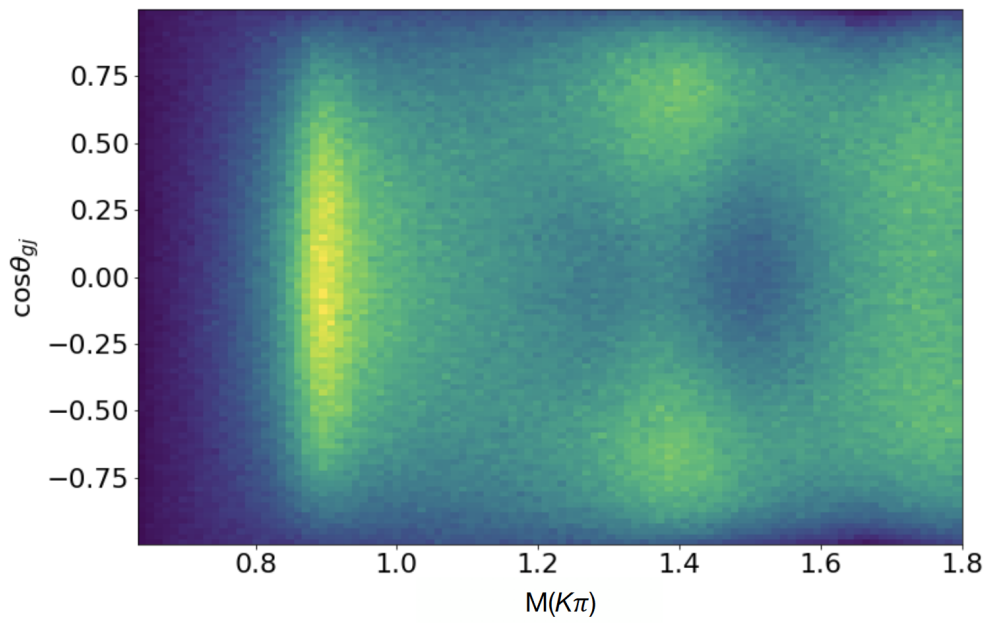


Figure 28: $\cos\theta_{GJ}$, cosine of the Gottfried-Jackson angle, as a function of the invariant mass $M(K\pi)$ in GeV.

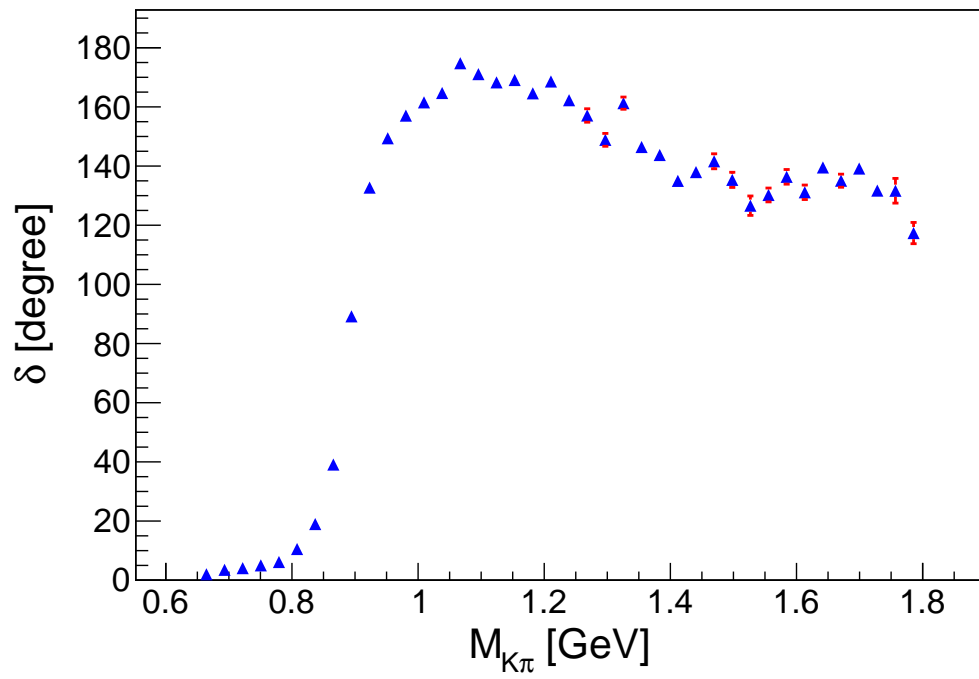


Figure 29: P -wave phase-shift distribution obtained by using Amptool [40].

8 SYSTEMATIC UNCERTAINTIES

Non- $K\pi$ scattering backgrounds are likely to play a role leading to systematic errors in the results of this analysis. One source of background could be the higher mass baryonic resonances in the case of $K^\pm\pi^\mp p$ final states. In the case when the final system is $K^-\pi^0\Delta^{++}$, one source of uncertainties is due to the background under the π^0 peak, which according to the current GlueX measurement [34] is estimated to be on the order of less than 1%, another source of systematic uncertainties is stemming from the K_L beam flux normalization systematics on the order of 5%. In the case of $\pi^-\Delta^{++}(K_L)$ in addition the uncertainty may come from the $\Lambda\pi^+(\pi^0)$ background, which should be vetoed by selecting events, where invariant mass of $p\pi^-$ lies above ground state $\Lambda(1116)$. Overall for the reactions with Δ^{++} we expect systematic uncertainties to be on the order $\sim 5\%$, while in the neutral pion exchange reactions systematic errors may be higher.

9 SUMMARY

As it is discussed in this note, there are many aspects of $K\pi$ scattering that require improvement on the existing measurements. First of all, it is the quest to establish existence or non-existence of scalar κ meson either to complete scalar meson nonet or to find an alternative way to explain well established non-strange σ , a_0 , and f_0 meson family. Besides there are some fundamental questions that need to be clarified. In particular, currently there is a sizable tension between the values of scattering lengths obtained from dispersive analyses of data [14, 15], on one side, and the predictions from Chiral Perturbation Theory [2, 3] and lattice calculations [5, 7, 9, 16], on the other side. The values of the threshold parameters are related to two important questions. On the one hand, for phenomenology, establishing the convergence and reliability of SU(3) Chiral Perturbation Theory. On the other hand, for the foundations of QCD, the size of the strange versus the non-strange chiral condensate, i.e., the detailed pattern of the QCD spontaneous chiral symmetry breaking is very important.

As previously noticed the existing SLAC data on $K\pi$ scattering start at 750 MeV, and one needs an extrapolation down to the threshold at ~ 635 MeV. Hence, the new KLF data at low energies, together with the general improvement in statistics, will be determinant to resolve this tension.

A Appendices

A.1 Generation Model For Monte Carlo Study

For the MC generation model, we used the t -dependence of the amplitude L_λ^\pm for production of $K\pi$ state of mass M , center-of-mass momentum q , angular momentum L , and t -channel helicity λ , by natural and unnatural parity exchange [19, 38],

$$\begin{aligned}
 L_0 &= \frac{\sqrt{-t}}{m_\pi^2 - t} G_{K\pi^+}^L(m_{K\pi}, t) , \\
 L_1^- &= \sqrt{\frac{L(L+1)}{2}} G_{K\pi^+}^L(m_{K\pi}, t) \gamma_c(m_{k\pi}) \exp(b_c(m_{k\pi})(t - m_\pi^2)) , \\
 L_1^+ &= \sqrt{\frac{L(L+1)}{2}} G_{K\pi^+}^L(m_{K\pi}, t) \left[\gamma_c(m_{k\pi}) e^{b_c(m_{k\pi}) \cdot (t - m_\pi^2)} - 2i \gamma_a(m_{k\pi}) e^{b_a(m_{k\pi}) \cdot (t - m_\pi^2)} \right] , \\
 L_\lambda^\pm &= 0, \lambda \geq 2 ,
 \end{aligned} \tag{12}$$

where $G_{K\pi}^L$ is related to the $K\pi$ elastic scattering amplitude a_L by

$$G_{K\pi^+}^L(m_{K\pi}, t) = N \frac{m_{K\pi}}{\sqrt{q}} a_L(m_{K\pi}) e^{b_L(m_{k\pi}) \cdot (t - m_\pi^2)} . \tag{13}$$

Here N is the normalization factor and is determined by requiring the $K\pi$ P -wave in the 900 MeV region to be an elastic Breit-Wigner resonance. Other parameters are mass dependent and the values are reported in [38]. The value of a_L from Eq. (13) in the elastic region is,

$$a_L^I = \sqrt{(2L+1)} \epsilon^I \sin \delta_L^I e^{\delta_L^I} , \tag{14}$$

and in inelastic region is

$$a_L = |a_L| e^{i\phi_L} . \tag{15}$$

The intensity $|a_L|$ and the phase ϕ_L values are taking from the dispersive calculation in Ref. [39]. The production amplitude L_λ^\pm is then used as a model to generate the Monte Carlo events. The first two panels on Fig. 30 show $I = \frac{1}{2}$ intensity and phase distributions for S -, P -, and D -waves respectively. Whereas the last panel is a phase distribution for $I = \frac{3}{2}$ S wave.

For recoil Δ^{++} , the production amplitudes are in Eq. (16), where $L_{\Delta N}^{\lambda\pm}$ is use to represent the amplitude for angular momentum L , helicity λ , $K\pi$ production by natural (+) and unnatural (-) parity exchange with Δ helicity and proton helicity N .

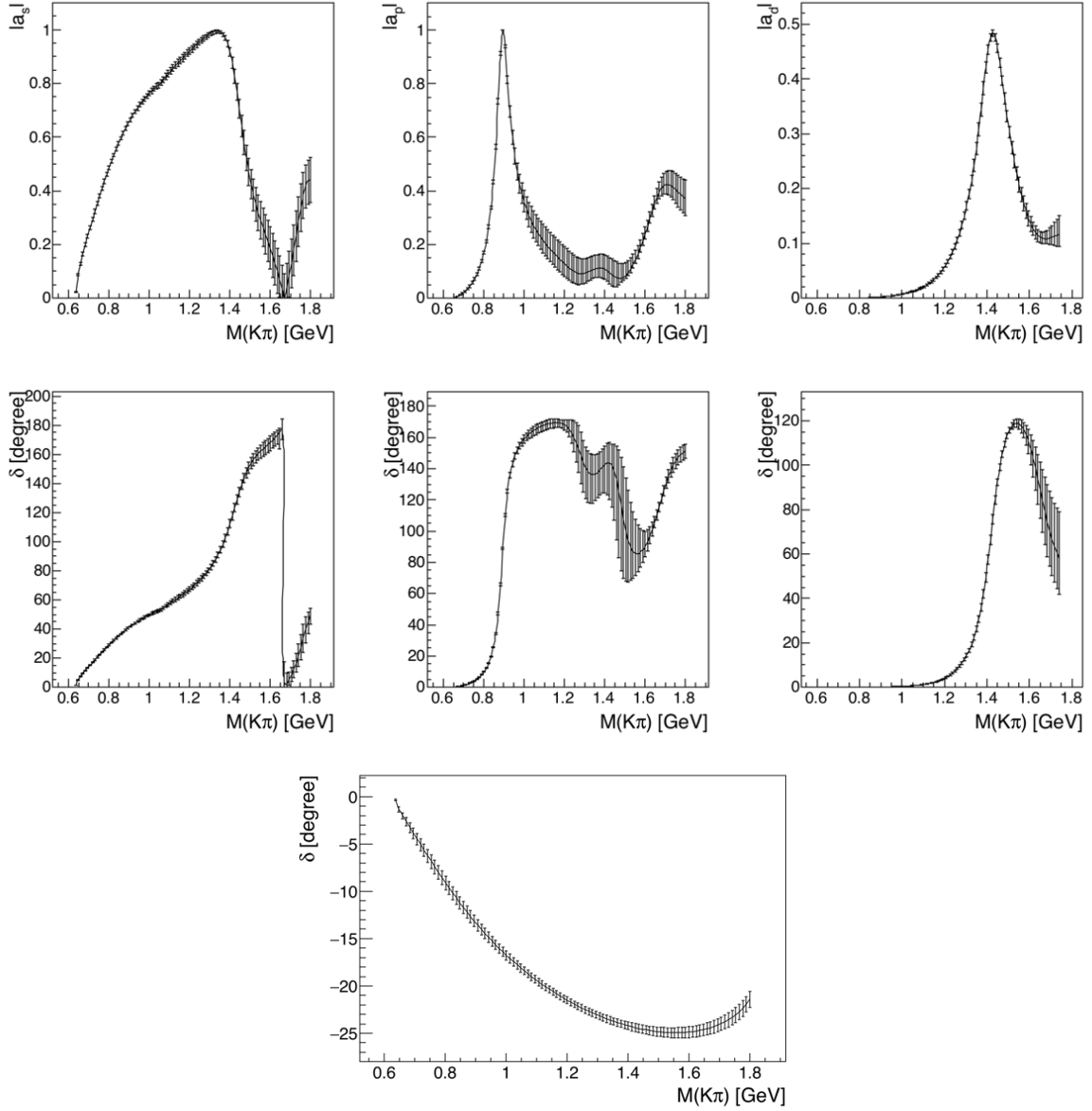


Figure 30: Intensity and Phase distribution calculated from the dispersive analysis (Ref. 30). Top row: Intensity distributions for S -, P - and D -waves of $I = 1/2$. Middle row: Corresponding phase shifts. Bottom row: Phase shift distribution for $I = 3/2$ S -wave.

$$\begin{aligned}
 L_{1+}^0 &= g_L \frac{\sqrt{(M_\Delta - M_N)^2 - t}}{\mu^2 - t}, \\
 L_{1-}^{1+} &= \frac{1}{\sqrt{3}} L_{3+}^{1+} = \sqrt{2} \gamma_A(-t') \sqrt{L(L+1)} g_L,
 \end{aligned} \tag{16}$$

where g_L is,

$$g_L = N \frac{M_{K\pi}}{\sqrt{q}} a_L e^{b_L(t-\mu^2)} . \quad (17)$$

Here a_L is the $K\pi$ scattering amplitude, N is normalization constant which can be determined by assuming a P -wave in 900 MeV $K\pi$ mass region to the elastic Breit-Wigner resonance.

References

- [1] V. Bernard, N. Kaiser, and U. G. Meißner, “pi K scattering in chiral perturbation theory to one loop,” Nucl. Phys. B **357**, 129 (1991).
- [2] V. Bernard, N. Kaiser, and U. G. Meißner, “Threshold parameters of pi K scattering in QCD,” Phys. Rev. D **43**, 2757 (1991).
- [3] J. Bijnens, P. Dhonte, and P. Talavera, “pi K scattering in three flavor ChPT,” JHEP **0405**, 036 (2004).
- [4] C. Miao, X. i. Du, G. w. Meng, and C. Liu, “Lattice study on kaon pion scattering length in the $I = 3/2$ channel,” Phys. Lett. B **595** 400-407 (2004).
- [5] S. R. Beane *et al.*, “pi K scattering in full QCD with domain-wall valence quarks,” Phys. Rev. D **74**, 114503 (2006).
- [6] J. Nagata, S. Muroya, and A. Nakamura, “Lattice study of K pi scattering in $I = 3/2$ and $1/2$,” Phys. Rev. C **80**, 045203 (2009).
- [7] Z. Fu, “Lattice study on πK scattering with moving wall source,” Phys. Rev. D **85**, 074501 (2012).
- [8] C. B. Lang, L. Leskovec, D. Mohler, and S. Prelovsek, “K pi scattering for isospin $1/2$ and $3/2$ in lattice QCD,” Phys. Rev. D **86**, 054508 (2012).
- [9] K. Sasaki *et al.* [PACS-CS Collaboration], “Scattering lengths for two pseudoscalar meson systems,” Phys. Rev. D **89**, no. 5, 054502 (2014).
- [10] D. J. Wilson, J. J. Dudek, R. G. Edwards, and C. E. Thomas, “Resonances in coupled $\pi K, \eta K$ scattering from lattice QCD,” Phys. Rev. D **91**, no.5, 054008 (2015).
- [11] C. Helmes *et al.* [ETM Collaboration], “Hadron-Hadron Interactions from $N_f = 2+1+1$ Lattice QCD: $I = 3/2$ πK Scattering Length,” Phys. Rev. D **98**, no.11, 114511 (2018).
- [12] C. K. Guruswamy, U. G. Meißner and C. Y. Seng, “Contraction Diagram Analysis in Pion-Kaon Scattering,” [arXiv:2002.01763 [hep-lat]].
- [13] V. Bernard, “First determination of $f_+(0)|V_{us}|$ from a combined analysis of $\tau \rightarrow K\pi\nu_\tau$ decay and πK scattering with constraints from $K_{\ell 3}$ decays,” JHEP **1406**, 082 (2014).
- [14] P. Büttiker, S. Descotes-Genon, and B. Moussallam, “A new analysis of pi K scattering from Roy and Steiner type equations,” Eur. Phys. J. C **33**, 409 (2004).

- [15] J.R. Pelaez *et al.*, “Pion-kaon scattering amplitude constrained with forward dispersion relations up to 1.6 GeV,” *Phys. Rev. D* **93**, 074025 (2016).
- [16] J. M. Flynn and J. Nieves, “Elastic s-wave B pi, D pi, D K and K pi scattering from lattice calculations of scalar form-factors in semileptonic decays,” *Phys. Rev. D* **75**, 074024 (2007).
- [17] J. R. Batley *et al.* [NA48-2 Collaboration], “Precise tests of low energy QCD from K(e4)decay properties,” *Eur. Phys. J. C* **70**, 635-657 (2010).
- [18] J. R. Pelaez, “From controversy to precision on the sigma meson: a review on the status of the non-ordinary $f_0(500)$ resonance,” *Phys. Rept.* **658**, 1 (2016).
- [19] P. Estabrooks, R. K. Carnegie, A. D. Martin, W. M. Dunwoodie, T. A. Lasinski, and D. W. G. S. Leith, “Study of $K\pi$ scattering using the reactions $K^\pm p \rightarrow K^\pm \pi^+ n$ and $K^\pm p \rightarrow K^\pm \pi^- \Delta^{++}$ at 13-GeV/c,” *Nucl. Phys. B* **133**, 490 (1978).
- [20] A. Dobado and J. R. Pelaez, “A global fit of pi pi and pi K elastic scattering in ChPT with dispersion relations,” *Phys. Rev. D* **47**, 4883 (1993).
- [21] J. A. Oller and E. Oset, “Chiral symmetry amplitudes in the S wave isoscalar and isovector channels and the σ , $f_0(980)$, $a_0(980)$ scalar mesons,” *Nucl. Phys. A* **620**, 438 (1997); Erratum: [*Nucl. Phys. A* **652**, 407 (1999)].
- [22] M. Jamin, J. A. Oller, and A. Pich, “S wave K pi scattering in chiral perturbation theory with resonances,” *Nucl. Phys. B* **587**, 331 (2000).
- [23] A. Gomez Nicola and J. R. Pelaez, “Meson meson scattering within one loop chiral perturbation theory and its unitarization,” *Phys. Rev. D* **65**, 054009 (2002).
- [24] J. Nebreda and J. R. Pelaez, “Strange and non-strange quark mass dependence of elastic light resonances from SU(3) Unitarized Chiral Perturbation Theory to one loop,” *Phys. Rev. D* **81**, 054035 (2010).
- [25] Z. H. Guo and J. A. Oller, “Resonances from meson-meson scattering in U(3) CHPT,” *Phys. Rev. D* **84**, 034005 (2011).
- [26] A. V. Anisovich and A. V. Sarantsev, “K matrix analysis of the K pi S wave in the mass region 900-MeV - 2100-MeV and nonet classification of scalar q anti-q states,” *Phys. Lett. B* **413**, 137 (1997).

- [27] C. Cawfield *et al.* [CLEO Collaboration], “Measurement of interfering $K^{*+} K^-$ and $K^{*0} K^+$ amplitudes in the decay $D^0 \rightarrow K^+ K^- \pi^0$,” *Phys. Rev. D* **74**, 031108 (2006).
- [28] R. Delbourgo and M. D. Scadron, “Dynamical generation of linear sigma model SU(3) Lagrangian and meson nonet mixing,” *Int. J. Mod. Phys. A* **13**, 657 (1998).
- [29] M. D. Scadron, F. Kleefeld, G. Rupp, and E. van Beveren, “Meson form-factors and the quark level linear sigma model,” *Nucl. Phys. A* **724**, 391 (2003).
- [30] Z. Y. Zhou and H. Q. Zheng, “An improved study of the kappa resonance and the non-exotic s wave πK scatterings up to $\sqrt{s} = 2.1$ GeV of LASS data,” *Nucl. Phys. A* **775**, 212 (2006).
- [31] E. M. Aitala *et al.* [E791 Collaboration], “Dalitz plot analysis of the decay $D^+ \rightarrow K^- \pi^+ \pi^+$ and indication of a low-mass scalar $K \pi$ resonance,” *Phys. Rev. Lett.* **89**, 121801 (2002).
- [32] J. Z. Bai *et al.* [BES Collaboration], “Evidence of kappa particle in $J/\psi \rightarrow \text{anti-}K^*(892)^0 K^+ \pi^-$,” hep-ex/0304001.
- [33] A. I. Titov and T. S. H. Lee, “Spin effects and baryon resonance dynamics in φ -meson photoproduction at few GeV,” *Phys. Rev. C* **065205**, 67 (2003).
- [34] S. Adhikari *et al.* [GlueX Collaboration], “The GlueX beam line and detector,” in progress.
- [35] D. V. Dass and C. D. Froggatt, “Regge-pole model for vector meson production (II) the reaction $KN \rightarrow K^*N$,” *Nuclear Physics B* **151**, 10 (1969).
- [36] J. H. Friedman and R. R. Ross, “Production and decay properties of the $K_0(892)$ produced in the reaction $K^- p \rightarrow \text{anti-}K_0 \pi^+ n$ At 2.1-GeV/c, 2.45-GeV/c, and 2.64-GeV/c,” *Phys. Rev. Lett.* **16**, 485 (1966).
- [37] M. Bashkanov, N. Zachariou, K. Park, S. Taylor, and I. Strakovsky, “Analysis report on KLF hyperon spectroscopy,” Preprint, 2020.
- [38] D. Aston *et al.*, “A study of $K^- \pi^+$ scattering in the reaction $K^- p \rightarrow K^- \pi^+ n$ at 11 GeV/c,” *Nucl. Phys. B* **296**, 493 (1988).
- [39] J.R. Pelaez, and A. Rodas, “Determination of the Lightest Strange Resonance $K_0^*(700)$ or κ , from a Dispersive Data Analysis,” *Phys. Rev. Lett.* **124**, 172001 (2020).

- [40] “<https://github.com/mashephe/AmpTools/wiki>”
- [41] J. Peláez and A. Rodas, “Determination of the lightest strange resonance $K_0^*(700)$ or κ , from a dispersive data analysis,” *Phys. Rev. Lett.* **124**, no.17, 172001 (2020).
- [42] J. R. Peláez and A. Rodas, in preparation.
- [43] M. Amaryan, C. Meyer, U.-G. Meißner, J. Ritman, and I. Strakovsky, eds., Mini-Proceedings, *Workshop on Pion-Kaon Interactions* (PKI2018); arXiv:1804.06528 [hep-ph].
- [44] M. Tanabashi *et al.* [Particle Data Group], “Review of Particle Physics,” *Phys. Rev. D* **98**, no. 3, 030001 (2018).